HOSTED BY
ELSEVIER

Available online at www.sciencedirect.com

ScienceDirect

Soils and Foundations 65 (2025) 101627

SOILS AND FOUNDATIONS

www.elsevier.com/locate/sandf

Technical Paper

Load transfer behaviour of super long piles in multi-layer soft soil through field testing and numerical 3D FEM modelling

Thoi Huu Tra [a], Thanh T. Nguyen [b,*], Thien Q. Huynh [b], Tatsuya Ishikawa [c]

[a] *International College of Ho Chi Minh City, Viet Nam*
[b] *Transport Research Centre (TRC) & School of Civil and Environmental Engineering, University of Technology Sydney, Australia*
[c] *Faculty of Engineering, Hokkaido University, Japan*

Received 12 December 2024; received in revised form 9 April 2025; accepted 3 May 2025

Abstract

The load transfer mechanism of pile foundation has received considerable attention over the years, the simultaneous responses that skin friction and base resistances of super-long piles (length $L > 60$ m) can have in complex soft soil, however, still need greater understanding. This study employs 3D-finite element (FE) analysis incorporating virtual interface elements to simulate the mobilised skin friction and plastic failure (slippage) of pile under ultimate loading. Static pile load tests on 4 different long and large bored piles (1–1.5 m in diameter and 70–80 m in length) embedded in the soft soil region of Mekong Delta are studied in detail through extensive instrumentation along the piles. The results are then used to not only explore load-transfer process, but also validate numerical modelling through a comprehensive process combining multiple-soil layers and −loading stages. The coupled experimental (field) − numerical results reveal the predominant contribution of skin friction exceeding 90 % of the entire bearing capacity before a drop with swift rise in base resistance when reaching a critical condition (displacement $s_h > 25$ mm and load pressure $p > 14{,}000$ kPa). The ratio of active skin friction is defined to assess the simultaneous variation of skin friction at different depths, featuring the role of pile length on the mobilisation of skin friction. The study also proposes a novel dynamic method to calculate the strength reduction factor, R_i, based on fundamental soil and load parameters, giving a vital means to advancing the use of interface elements when modelling pile foundation in soft soil.

Keywords: Finite element modelling; Interface elements; Load transfer; Pile foundation; Skin friction; Base resistance; Strength reduction factor

1. Introduction

Pile foundation has become one of the most effective solutions for high-rise buildings and infrastructure (e.g., energy, coastal and transportation) around the world (Galvín et al. 2017; Nguyen et al. 2022; Shaolei et al. 2015). As this foundation can support heavy loads and effectively minimise settlement, it is notably favourable in weak soft soil regions such as the Mekong Delta (the South of Vietnam). For example, there were a myriad of super-large and −long bored piles (diameter D = 1–2.5 m and length L = 50–100 m) used to carry massive loads under towers and buildings in Ho Chi Minh City situated in the edge of the Mekong Delta (Nguyen et al. 2024). The geological condition of Ho Chi Minh City is extremely sophisticated with a thick soft to very soft soil layer that can rise up to about 30 m as portrayed in Fig. 1 (Layer 1 and 2), giving significant challenges to having effective foundation designs. While previous studies often focus on short to medium piles, i.e., $L < 40$ m (Al-Atroush et al. 2020; Huynh et al. 2022b; Krasiński and Wiszniewski 2017), super-long piles embedded in complex soft soil strata requires better understanding.

* Corresponding author.
E-mail address: thanh.nguyen-4@uts.edu.au (T.T. Nguyen).

https://doi.org/10.1016/j.sandf.2025.101627
0038-0806/© 2025 Japanese Geotechnical Society. Published by Elsevier B.V.

Nomenclature

A	cross-sectional area of pile	$Q_{s,\max}$	total shaft resistance at final load level
c	cohesion of soil	q_b	base resistance
c_i	cohesion of interface	q_s	unit skin friction
c'	effective cohesion of soil	R_i	strength reduction factor (R-inter)
D	pile diameter	$R_{i,m}$	mean strength reduction factor
e	void ratio	S_u	undrained shear strength
$d\tau$	incremental shear stress of interface	s_b	pile base displacement
$d\varepsilon$	incremental shear strain of interface	s_h	pile head displacement
E_{oed}	oedometer loading stiffness	s_s	pile shaft displacement
E_p	Elastic modulus of pile material	u	shear displacement of interface
E_{ur}	triaxial unloading stiffness	u_1	ultimate shear displacement of interface
E_{50}	triaxial loading stiffness	u_2	residual shear displacement of interface
E_{50}^{ref}	secant stiffness at the reference stress	γ	unit weight
G	shear modulus of interface	σ'_1	vertical effective stress at the middle of soil layer
G_s	shear modulus of soil	σ_3	horizontal effective stress
h	depth	τ	shear stress of interface
k_s	coefficient of mobilised skin friction	τ_f	ultimate shear strength of interface
L	pile length	τ_m	mobilised shear strength of interface
m	exponent	τ_{max}	shear strength at the middle of soil layer
N	SPT value	τ_r	residual shear strength of interface
P	axial load on pile head	φ	friction angle of soil
p_{ref}	reference stress	φ_i	friction angle of interface
p	pressure on pile head	φ'	effective friction angle of soil
$Q_{b,\max}$	total base resistance at final load level		

Subjected to an axial loading, pile transmits the load to the surrounding soil through skin friction along the pile shaft and base resistance (also known as end-bearing capacity) at the pile tip. The skin friction increases with rising relative displacement between pile and soil, exhibiting elasto-plastic transformation when it approaches the peak skin friction before falling into a residual stage (Hirayama 1990; Sharo et al. 2022). This process is usually termed as mobilisation of skin friction that propagates downward with increasing contribution from the lower parts to the entire bearing capacity of the pile. Meanwhile, the base resistance often takes minor role at initial stages and gradually increases when the displacement of pile reaches a certain degree. For example, a recent site investigation (Nguyen et al. 2024) on long piles ($L > 60$ m) in soft soil showed that the base resistance becomes significantly only when the settlement of piles > 0.1 % of the pile's length. These simultaneous responses of shaft and base resistances under increasing load are depicted in Fig. 2. For a given time, the pile shaft displacement (s_s) decreases over the depth (h) since the pile compression accumulates from the pile head to the tip under loading. This means that the upper elements of the pile such as Sections A and B can exhibit post-peak state (presented by black dots), whereas those closer to the pile tip (e.g., Section C) are approaching their peaks of skin resistance due to smaller magnitude of displacement. In the meantime, the base (tip) resistance slowly increases and only becomes apparent when the displacement is very large.

Various methods have been developed to simulate the load-transfer process as well as estimating shaft and base resistances of piles under axial loading. Among them, finite element method (FEM) has become one of the most preferrable options as it can incorporate advanced constitutive soil models and handle complex geometry (Abu-Farsakh et al. 2015; Hamderi 2018; Said et al. 2009; Tamboura et al. 2022). However, previous finite element (FE) modelling of pile foundation faced some crucial limitations that requires attention. Firstly, majority of past FE studies concentrated on reproducing the load–displacement curves (normally at the pile head), while ignoring the simultaneous behaviours of shaft and base resistances at different depths (Alwalan and El Naggar 2020; Amornfa and Sanguanduan 2023; Tra et al. 2023). Although efforts have been made to investigate soil-pile interactions, their models lack validation with relevant field tests such as using very short piles and/or without shaft and tip instrumentation (Al-Atroush et al. 2020; Krasiński and Wiszniewski 2017). These issues pose huge challenges for practical designers to select appropriate model parameters as well

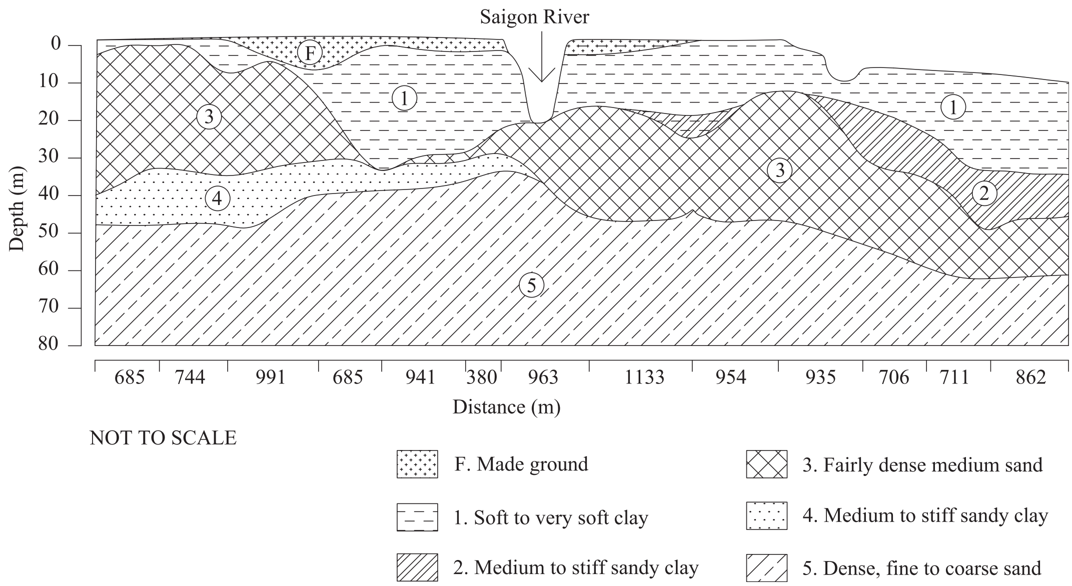

Fig. 1. Typical geological profile of Ho Chi Minh City around Saigon River - the major river in Mekong Delta.

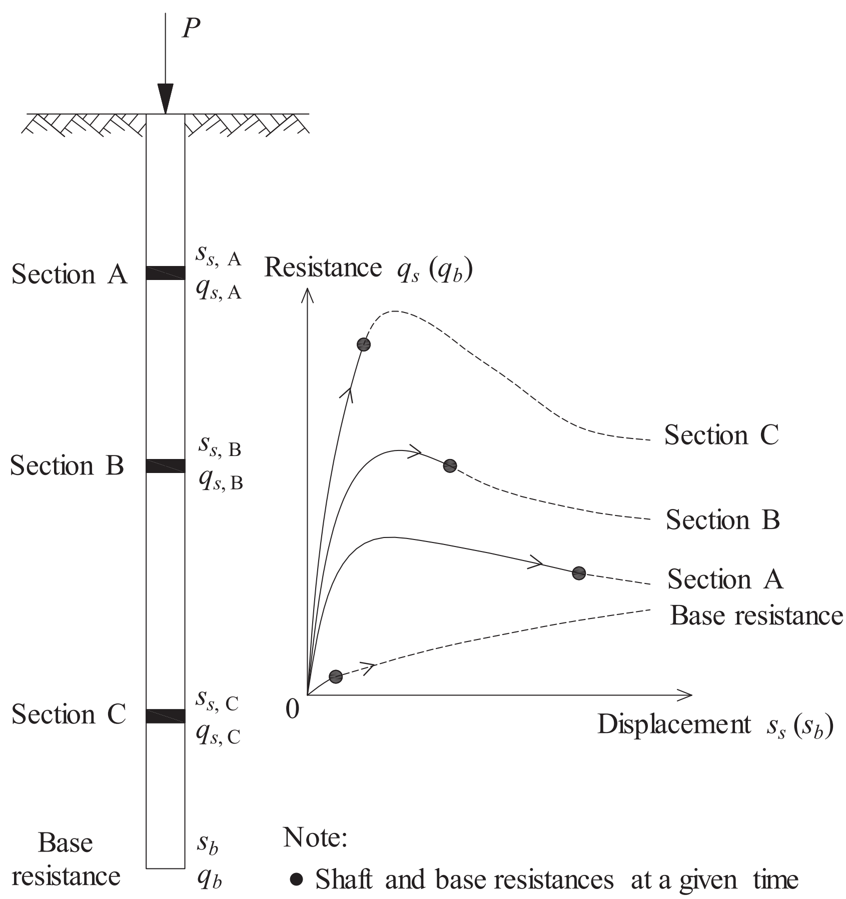

Fig. 2. Development of skin friction and base resistance with increasing displacement

as having proper understanding of load-transfer mechanism when long piles are installed in complex geological strata.

In FEM, the interaction between soil and structure elements can be simulated by using interface elements (joint elements). A major parameter defining these elements is the strength reduction factor, R-inter (R_i), which directly affects the magnitude of the pile-soil interface's shear strength and mobilised skin friction along the pile body. However, how to define value of this parameter has not been considered and understood properly. For example, Krasiński and Wiszniewski 2017 fixed the value of R_i, while others varied it dramatically based on direct shear tests for different types of soil, i.e., 0.34–0.8 (Ter-Martirosyan et al. 2019) and 0.39–0.57 (Sidorov and Almakaeva 2020). In fact, none has extensively investigated and characterised the value of R_i with reference to in-situ pile tests, especially for super-long piles in multilayer soil. This confusion has caused significant challenges in selecting appropriate value of R_i for FE models, requiring urgent attention.

In view of the above, the overarching aim of this study is twofold. Firstly, it substantially enhances our understanding of load-transfer behaviour of very long piles (70–80 m) installed in complex soft soil through extensive studies of field pile load tests and FE modelling. Secondly, it proposes a novel approach to determine value of the strength reduction factor R_i that significantly eases FE modelling. Four well-instrumented large and long bored piles in Ho Chi Minh City are selected, while 3D-volume piles are built using FEM to reproduce the load tests. The load-transfer process is characterised through a newly defined parameter, namely the ratio of skin friction. The unique feature of the current FE studies lies in the methodical and systematic validation of shaft (skin friction) and base resistances at different depths and loads with reference to the field test data. As a result, new empirical relationships between R_i and soil-pile and load features are generated, giving significant values to the practice of finite element FE modelling in deep foundation design.

2. Field load test on long piles in soft soil of Mekong Delta

2.1. Geological condition and project/site features

This study underwent 4 different high-rise building projects, i.e., Gia Phu (GP), Friendship Tower (FT), Vietcombank Tower (VT) and Ascent Plaza (AP) situated on the soft ground of Ho Chi Minh City, breeding a collection of 4 different super-large and –long-bored piles as summarized in Table 1. These piles had diameter between 1 m to 1.5 m and embedded depth up to approximately 80 m. They were installed in sophisticated geological strata as described in Fig. 3, causing complex behaviours of shaft (skin friction) and base resistances during loading process. The soft to very soft soil layers (SPT value $N < 10$), which would make insignificant contributions to the shaft resistance, reach up to 20 m in depth, causing significant challenges to foundation design. On the other hand, clayey sand and sand with $N > 30$ are predominant under 50 m depth. Stiff soils with $N > 50$ are only available at a $h > 70$ m (dense clayey sand and dense sand), which is also the depth often required for pile embedment in Mekong Delta. It is noteworthy that some soil layers might have similar geotechnical properties, such as the void ratio and Atterberg's limits of soil Layer 3_a, Pile GP and those in Layer 5_d, Pile AP, but show different values of SPT. This is because they are located at different depths, thus subjected to different confining pressures that significantly influenced SPT values. In addition, the test sites were located at low-lying area of Mekong Delta, the water table was usually about 1–2 m below the ground surface according to site investigation reports. Soils can therefore be assumed in fully saturated condition for most layers along the piles.

2.2. Static pile load tests and the results

Static load test (SLT) was conducted complying with ASTM standard (ASTM D1143 1981); their load-pile head displacement (P-s_h) curves are presented in Fig. 4. Piles GP, VT, and AP (Fig. 4a, c, and d, respectively) reach the critical state, where the pile head displacement rises steeply, for instance from 24 mm to nearly 90 mm in Pile VT (Fig. 4c), despite marginal increase of load. It is noteworthy that the term "critical point" might imply the yield load which marks a surge in displacement of pile under loading. In the current study, the critical point is used to identify failure state of pile that will benefit later analysis and discussion, the value of yield load is thus not estimated in detail in this study. The failure can be attributed to the substantial loss of skin friction from its peak in deeper soil layers (detailed later in Fig. 7a, c, and d), which led to the ever-increasing pressure on the pile tip, resulting in the swift growth of the pile displacement as shown later in Fig. 7e and f. By contrast, Pile FT (Fig. 4b) remains nearly in elastic stage as the skin friction at lower zones and the base resistance continue to increase steadily even at the largest load level, i.e., 30,000kN (Fig. 7b and e). Therefore, Piles GP, VT, and AP can be considered as representatives for failure cases, whereas Pile FT can be categorized into non-failure pile and well satisfied the design target (Table 1). Furthermore, the largest displacement of pile head relative to the pile diameters, as depicted in Fig. 4, show that this value for failure piles (Pile GP, VT, and

Table 1
Basic information of the four tested piles.

Bored pile Project	GP Gia Phu	FT Friendship Tower	VT Vietcombank Tower	AP Ascent Plaza
Diameter, D (m)	1.2	1.5	1.5	1.0
Length, L (m)	80	79	70.8	70.3
Designed load (kN)	12,000	15,000	14,000	90,00
Field test load (final load level) (kN)	26,400	30,000	26,040	11,700

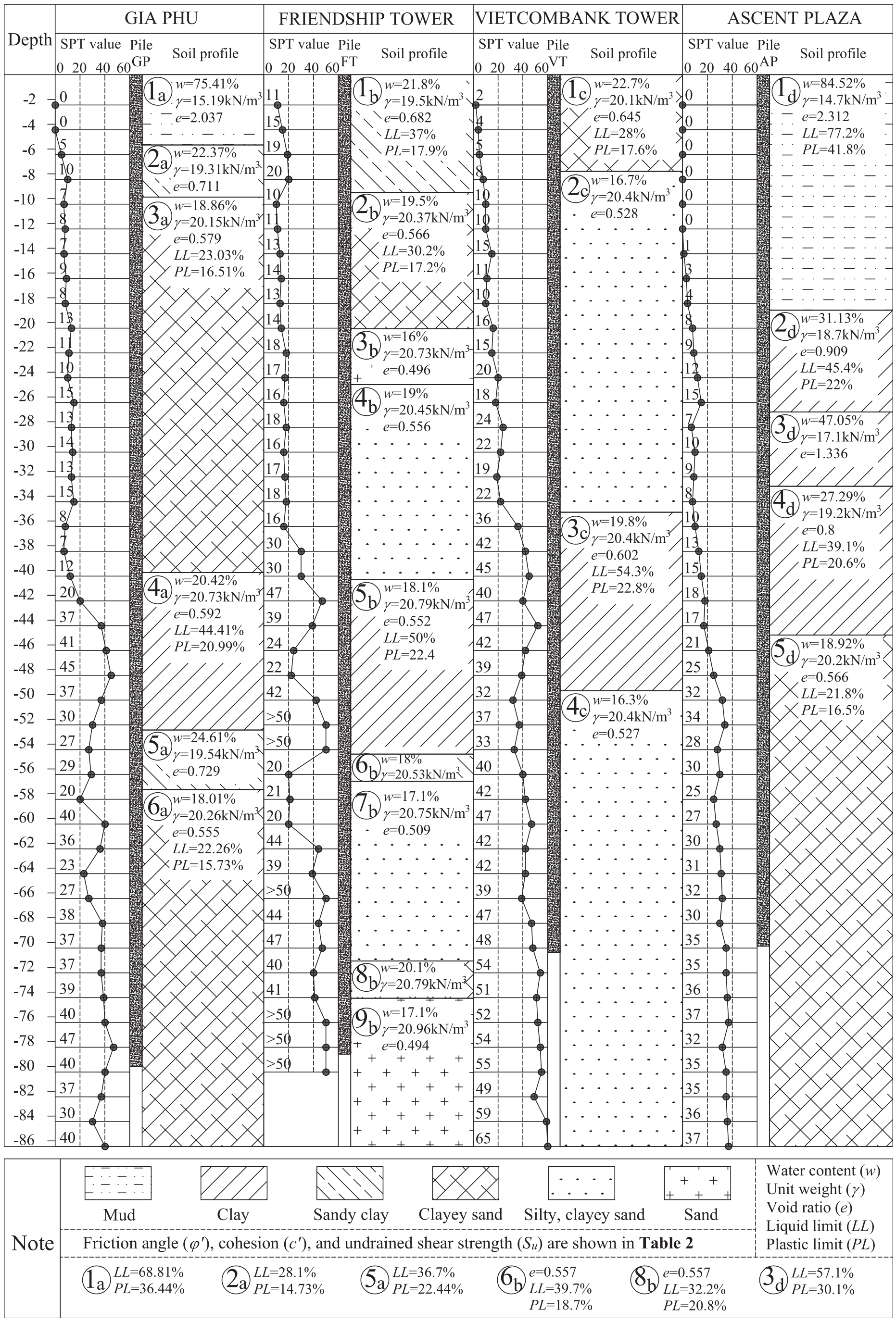

Fig. 3. Soil profile of the four selected pile tests in Ho Chi Minh City, Mekong Delta.

AP) exceeded 5.5 %×D, whereas it was just around 2.2 %×D for non-failure Pile FT.

In order to measure the mobilisation of the shaft and base resistances, strain gauges distributed at different soil layers were attached to steel reinforcement bars along the pile. The procedure to calculate skin friction from the strain gauge measurement is presented in Fig. 5. The axial forces at these cross-sections were computed based on the measured strain of steel bars through different loading stages (Fig. 6). It is noted that the term "Zone", which differs from the term "Layer" used earlier for soil classification, refers to the area between two consecutive strain gauges or between the ground and the first layer of strain gauges. Moreover, the base resistance was estimated using data from the strain gauges near to the pile toe (i.e., 0.3–1 m above the pile tip). Subsequently, the total shaft resistance due to surrounding soil acting on pile segments was the force disparity between two adjacent cross-sections. Fig. 7 shows the final results related to unit skin friction and base resistance.

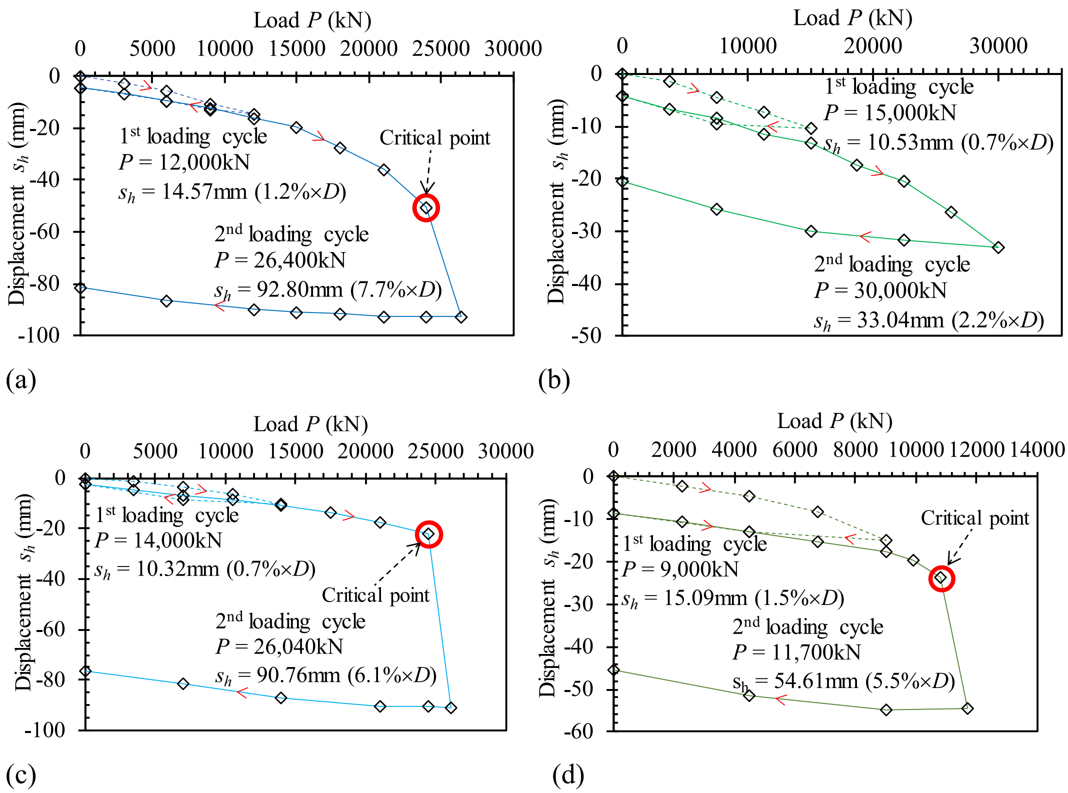

Fig. 4. Load - displacement curves: (a) Pile GP; (b) Pile FT; (c) Pile VT; (d) Pile AP.

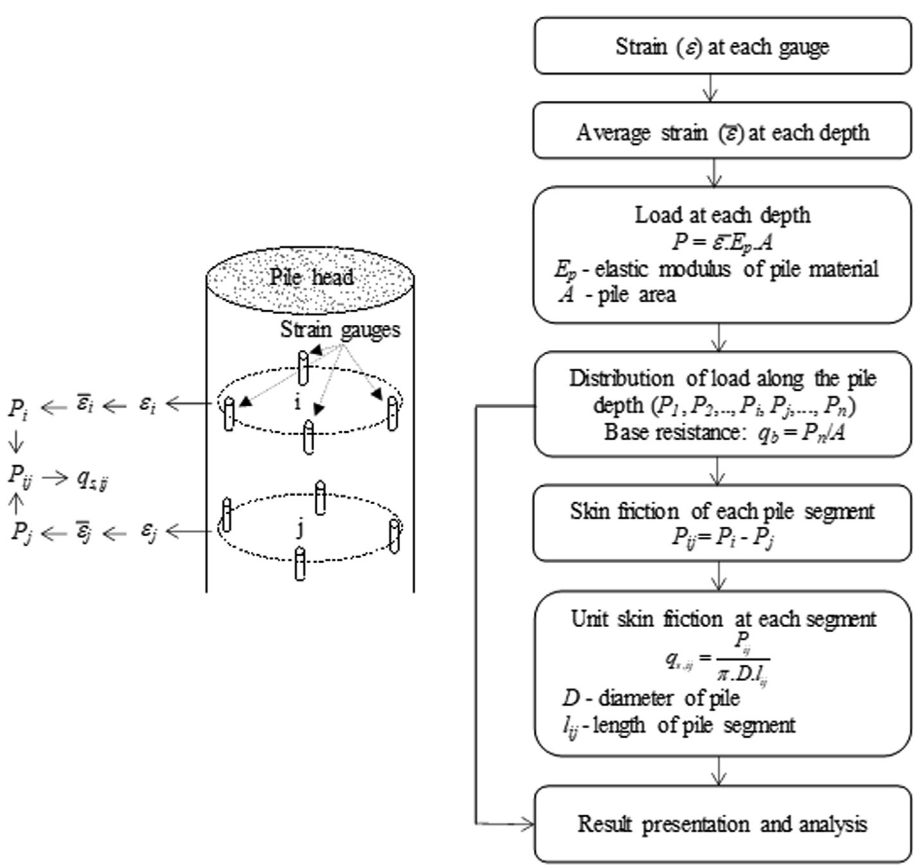

Fig. 5. Flow chart of stress–strain analysis using strain gauge measurement data from pile load tests.

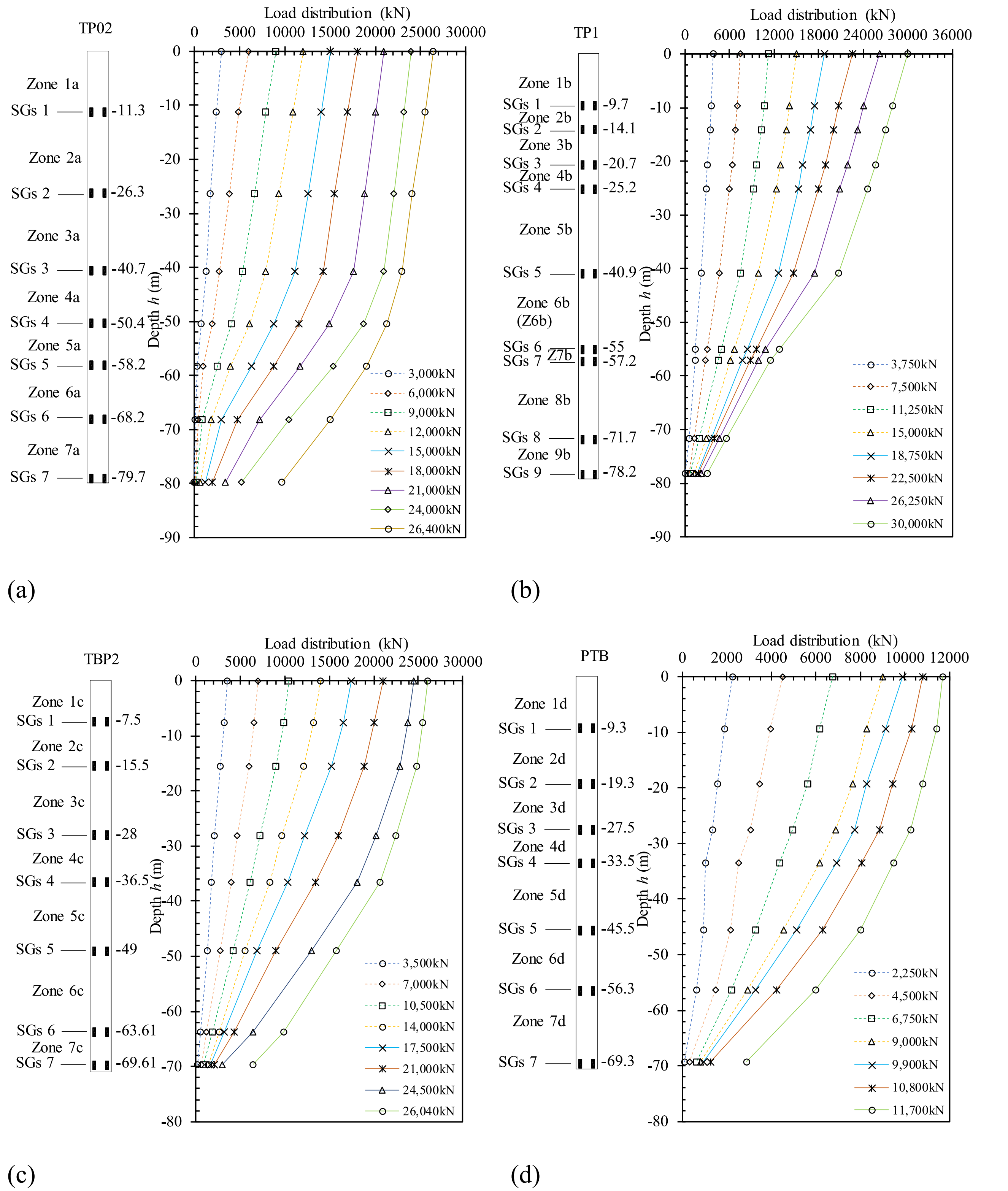

Note: SGs – Strain gauges

Fig. 6. Strain gauges arrangement and load distribution along the pile length: (a) Pile GP; (b) Pile FT; (c) Pile VT; (d) Pile AP.

Fig. 6 represents how the applied load is borne by the skin friction and base resistance cross 4 different test cases. When the load is small, for instance under 12,000kN (dashed lines), skin friction along the upper half of the pile takes majority of the load while the contributions from the lower parts are marginal. As the load increases, the skin friction from deeper segments of the piles takes bigger role that widens the distribution curve at the $h > 30$ m. For failure piles, such as Pile GP and Pile AP, there are surges in the base resistance at the final loading step, indicating the failure state where the skin friction substantially drops with dominant slippage (debonding stage) between soil and pile. On the other hand, the non-failure pile, Pile FT did not reach the failure yet as the load was terminated due to the satisfaction of designed target. As a result, the contributions from the lower parts are still small with the predominance of linear elastic behaviour.

Greater details of skin friction behaviour at individual layers are presented in Fig. 7a-d for the 4 investigated piles. The skin friction increases under loading and reaches the peak (maximum value) before decreasing to a residual level (debonding state with slippage). The deeper the soil-pile contact, the larger the skin resistance to loading, thus the higher the peak unit skin friction. For example, Fig. 7a shows that the unit skin friction of the first soft soil layers (Zone 1 to 3, $h < 40$ m including mud, clays and clayey sands) reaches a peak of only 24 kPa, whereas it can increase by a factor of 5–6 to approximately 120–130 kPa

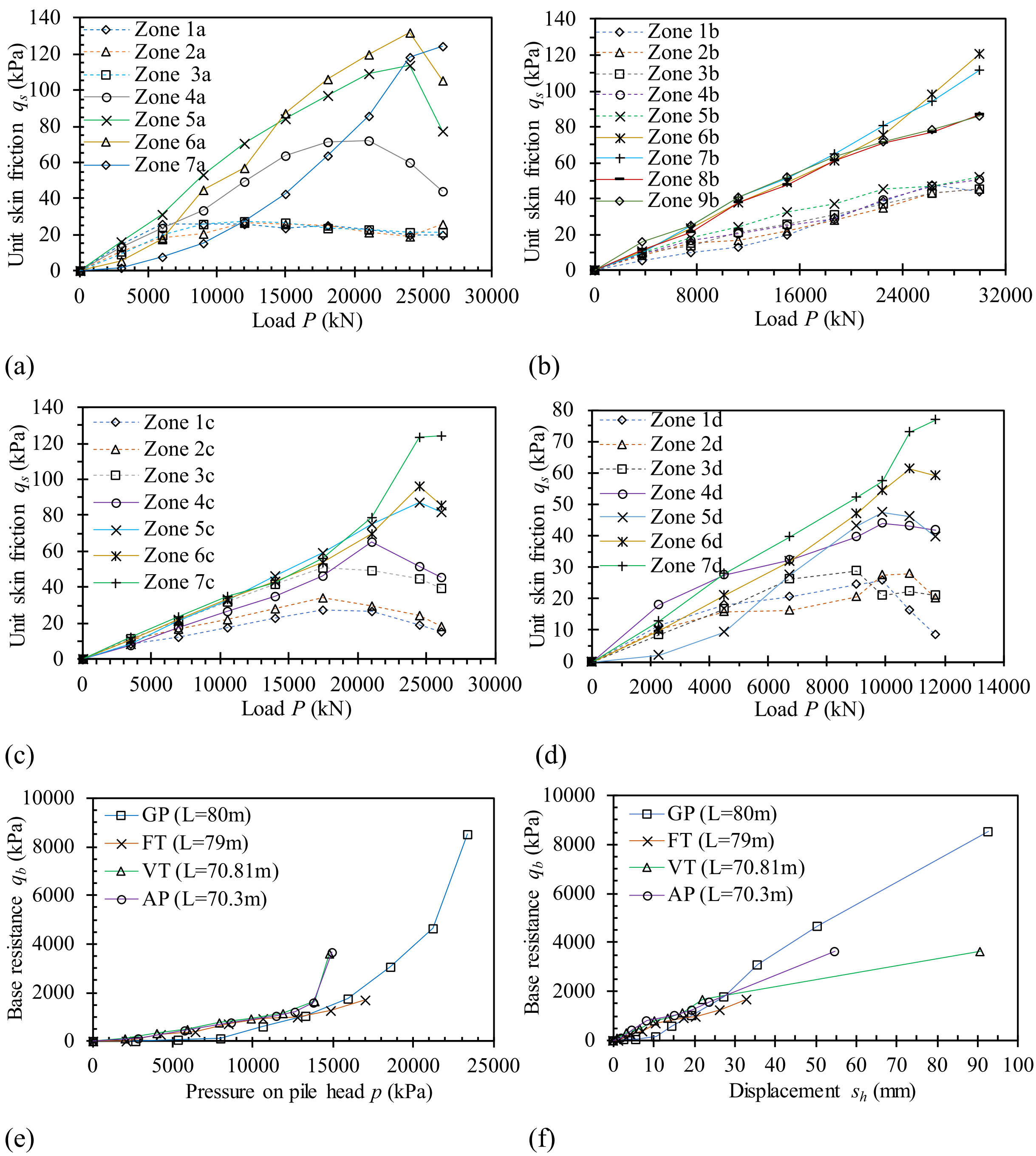

Fig. 7. Skin (shalf) and base resitances gained from static load tests: (a)-(d) Unit skin friction-load for Pile GP, FT, VT and AP; (e) Base resistance-pressure on pile head; (f) Base resistance-pile head displacement; (g) Comparison of unit skin friction between design calculation and field test.

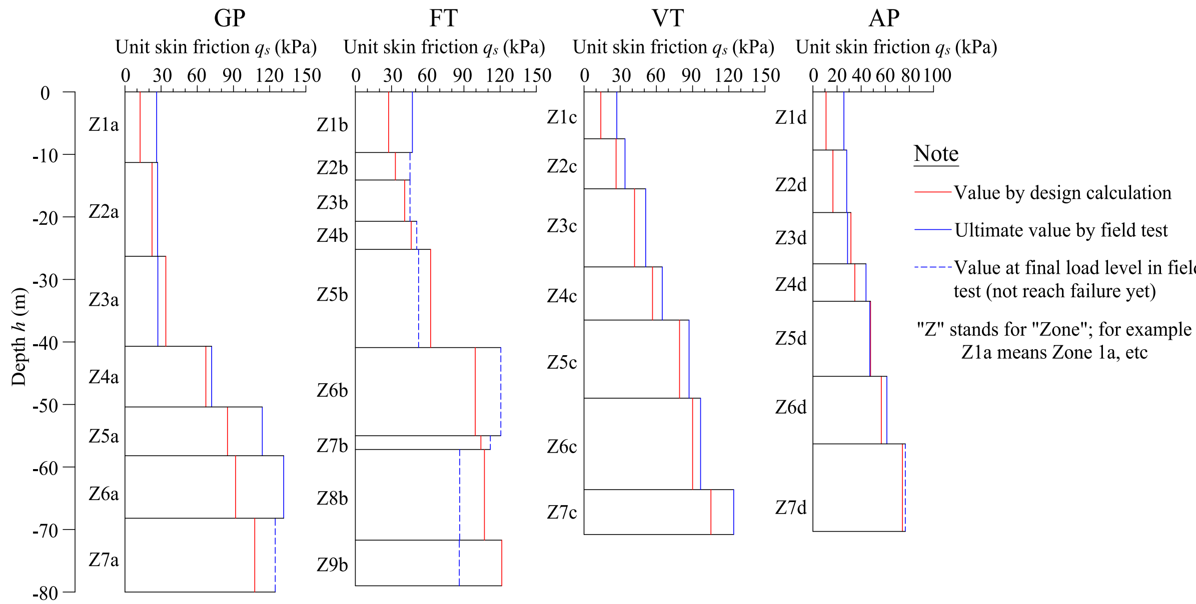

(g)

Fig 7. *(continued)*

for deeper soils. This was because of not only the stiffer soils (clayey sand to sand, void ratio from 0.49 to 0.55), but also the larger confining pressure that deeper layers had. Furthermore, the maximum unit skin friction within the lower zones of Pile AP (Fig. 7d) is significantly smaller than those of the remaining piles (Fig. 7a-c), i.e., approximately 80 kPa compared to 120 kPa. This can be explained by the fact that the soils in the lower zones around Pile AP are weaker than those in the other piles, as shown by the SPT values in Fig. 3. The N value of the lower soils (h = 35–80 m) in Pile AP is in the range 30–35, which is smaller than 40–50 in the counterparts. The mobilisation of base resistance with increasing pressure and displacement of pile head is depicted in Fig. 7e and f. For failure piles (Piles GP, VT, and AP), the base resistance linearly increases before an exponential growth. In contrast, the base resistance of non-failure Pile FT continues to rise steadily throughout the loading process. Further details will be explored later in conjunction with numerical insights in this paper. Furthermore, a comparison of the unit skin friction between the design calculation (TCVN 10304 2014) and the field measurement is made (Fig. 7g) to understand any significant differences between the two approaches. For failure piles (GP, VT, and AP) across all the soil layers, the designed values are well smaller than the largest levels that the piles can reach according to field test data. Some layers, especially upper zones such as Zone 1a (Z1a) and Zone 1b (Z1b) witness even 40–50 % disparity between the designed and measured skin friction. The gap between designed and real ultimate values of skin friction seems to decrease over the depth. On the other hand, for the non-failure Pile FT, the measured values of unit skin friction, especially in the lower soil layers are smaller than the designed values, as the ultimate level had not been reached in this pile yet.

3. Numerical simulations of pile load test

3.1. Soil and pile parameters

This study employed 3D FEM incorporated in Plaxis (Bentley 2022) to simulate pile load tests. The method of volume pile was used as it can capture complex pile-soil interaction, accurate stress–strain distributions and non-linear material behaviours. As the bored piles were much stiffer than the surrounding soils, a linear elastic model was used with the elastic modulus of 35GPa (cast-in-situ concrete). The Hardening-Soil (HS) model an advanced soil model based on isotropic hardening (Schanz et al. 2019) was adopted. This model not only takes stress-dependent stiffness according to a power law into consideration, as presented in Eq. (1), but also facilitates the use of undrained shear strength (S_u) based on vane shear tests, cone penetration tests, and similar methods, according to the Undrained B method (Bentley 2022), unlike other soil models such as Soft soil, Cam-Clay, and Mohr-Coulomb models. Undrained analysis was carried out for all soil layers except sandy soils where high permeability can allow sufficient dissipation of excess pore water pressure during pile test. The triaxial loading stiffness E_{50}, triaxial unloading stiffness E_{ur}, and the oedometer loading stiffness E_{oed} were used. The values of E_{ur} and E_{oed} were assumed to be $3E_{50}$ and E_{50}, respectively (Teo and Wong 2012). The E_{50} was calculated from Eq. (1) with reference to the secant stiffness E_{50}^{ref} which was taken as $500S_u$ for clayey mud and soft clay (Likitlersuang et al. 2013; Lim et al. 2010) and 1,500 N-2,200 N for sand and semi-stiff to stiff clay (Hsiung and Dao 2014; Huynh et al. 2022a). The exponent m was assigned as 0.55 for sand, 0.75 for semi-stiff to stiff clay, and 0.9–1 for mud and soft clay (Janbu 1963; Von Soos 1990), as shown in Table 2.

$$E_{50} = E_{50}^{ref}\left(\frac{c'.\cos\varphi' + \sigma_3.\sin\varphi'}{c'.\cos\varphi' + p_{ref}.\sin\varphi'}\right)^m \tag{1}$$

where σ_3 is the horizontal effective stress; $p_{ref} = 100$ kPa is the reference stress; c' and φ' are the effective cohesion and friction angle of soil, respectively.

3.2. Theoretical consideration of interface elements and R-inter calibration approach

Interface elements were employed to simulate the virtual zone (enveloped by the two cyan lines as depicted in Fig. 8) of intensely shearing material at the contact between the pile and the surrounding soil (Bentley 2022). Without the interface elements, the pile and the surrounding soil are tied together, resulting in no relative displacement (i.e., slipping, gapping). The interface elements have pairs of nodes connecting the pile and the soil as such one node belongs to the pile and the other belongs to the soil. As a result, the interface elements allow for different displacements between the node pairs, triggering relative displacement between the pile and the surrounding soil under loading (Fig. 8b). It is noteworthy that in Fig. 8, the interface elements are portrayed with a finite thickness where the coordinates of each node pair are different for convenient understanding. In real computation, they are identical with zero thickness of the interface elements and the position of the interface elements' stress points coincides with the node pairs. Also in this study, the FE model considered delamination of interface elements due to normal stress in both tensile and compressive states. This allowed the contact between soil and pile to be restored when the normal stress changes from tensile to compressive state, for example when switching between loading, unloading to reloading stages.

The relationship between shear stress and strain of the interface is described by:

$$d\tau = G.d\varepsilon \tag{2}$$

Table 2
Input parameters of soils using Hardening-Soil (HS) model.

Test pile	Soil layer	Depth, h (m)	Mean of N	φ' (deg)	c' (kPa)	S_u (kPa)	E_{50}^{ref} (kPa)	m
GP	1_a. Clayey mud	0–5.8	–	–	–	9.4	4,673	1
	2_a. Soft sandy clay	5.8–10	–	–	–	43.1	21,531	0.9
	3.1_a. Medium dense clayey sand	10–26.3	11.1	28.15	1.6	–	1500 N-2200 N	0.55
	3.2_a. Medium dense clayey sand	26.3–40.3	12.7	28.15	1.6	–	1500 N-2200 N	0.55
	4_a. Semi-stiff to stiff clay	40.3–53	32.7	27.2	37.3	–	1500 N-2200 N	0.75
	5_a. Semi-stiff sandy clay	53–57.8	28.5	26.25	31	–	1500 N-2200 N	0.75
	6.1_a. Medium dense clayey sand	57.8–68.2	29.7	30.13	2.7	–	1500 N-2200 N	0.55
	6.2_a. Medium dense clayey sand	68.2–90	30.3	30.13	2.7	–	1500 N-2200 N	0.55
FT	1_b. Semi-stiff sandy clay	0–9.5	14.4	24.5	33.2	–	1500 N-2200 N	0.75
	2.1_b. Medium dense clayey sand	9.5–14.1	11	27.87	17.2	–	1500 N-2200 N	0.55
	2.2_b. Medium dense clayey sand	14.1–20.5	14	27.87	17.2	–	1500 N-2200 N	0.55
	3_b. Medium dense sand	20.5–25	17.8	29.88	10.5	–	1500 N-2200 N	0.55
	4_b. Medium dense clayey sand	25–40.7	18.4	29.08	14.7	–	1500 N-2200 N	0.55
	5_b. Stiff sandy clay	40.7–54.8	40.8	27.2	51	–	1500 N-2200 N	0.75
	6_b. Semi-stiff sandy clay	54.8–57	21.5	26.4	38.6	–	1500 N-2200 N	0.75
	7_b. Dense clayey sand	57–71.5	39.7	28.5	13.9	–	1500 N-2200 N	0.55
	8_b. Dense silty clayey sand	71.5–74.5	40.3	27.9	16.7	–	1500 N-2200 N	0.55
	9_b. Very dense well graded sand	74.5–87	56.1	34.5	9.7	–	1500 N-2200 N	0.55
VT	1_c. Loose clayey sand	0–7.8	5	26	10.5	–	1500 N-2200 N	0.55
	2.1_c. Loose to dense clayey sand	7.8–15.5	10.6	29.78	12.4	–	1500 N-2200 N	0.55
	2.2_c. Loose to dense clayey sand	15.5–28	15.3	29.78	12.4	–	1500 N-2200 N	0.55
	2.3_c. Loose to dense clayey sand	28–35.3	21.1	29.78	12.4	–	1500 N-2200 N	0.55
	3_c. Stiff clay	35.3–49.7	40	28.5	35.5	–	1500 N-2200 N	0.75
	4.1_c. Medium to very dense sand	49.7–63.6	37.8	30.03	12.2	–	1500 N-2200 N	0.55
	4.2_c. Medium to very dense sand	63.6–80	46.8	30.03	12.2	–	1500 N-2200 N	0.55
AP	1.1_d. Clayey mud	0–9.3	–	–	–	8.9	4,460	1
	1.2_d. Clayey mud	9.3–19	–	–	–	17.9	8,975	1
	2_d. Stiff clay	19–27.2	12.7	26.83	31.1	–	1500 N-2200 N	0.75
	3_d. Semi-stiff clay	27.2–33.2	9.8	24.68	23.7	–	1500 N-2200 N	0.75
	4_d. Stiff clay	33.2–45.2	14.9	28.25	27.1	–	1500 N-2200 N	0.75
	5.1_d. Medium dense clayey sand	45.2–56.3	28.1	30.2	11.5	–	1500 N-2200 N	0.55
	5.2_d. Medium dense clayey sand	56.3–80	32.9	30.2	11.5	–	1500 N-2200 N	0.55

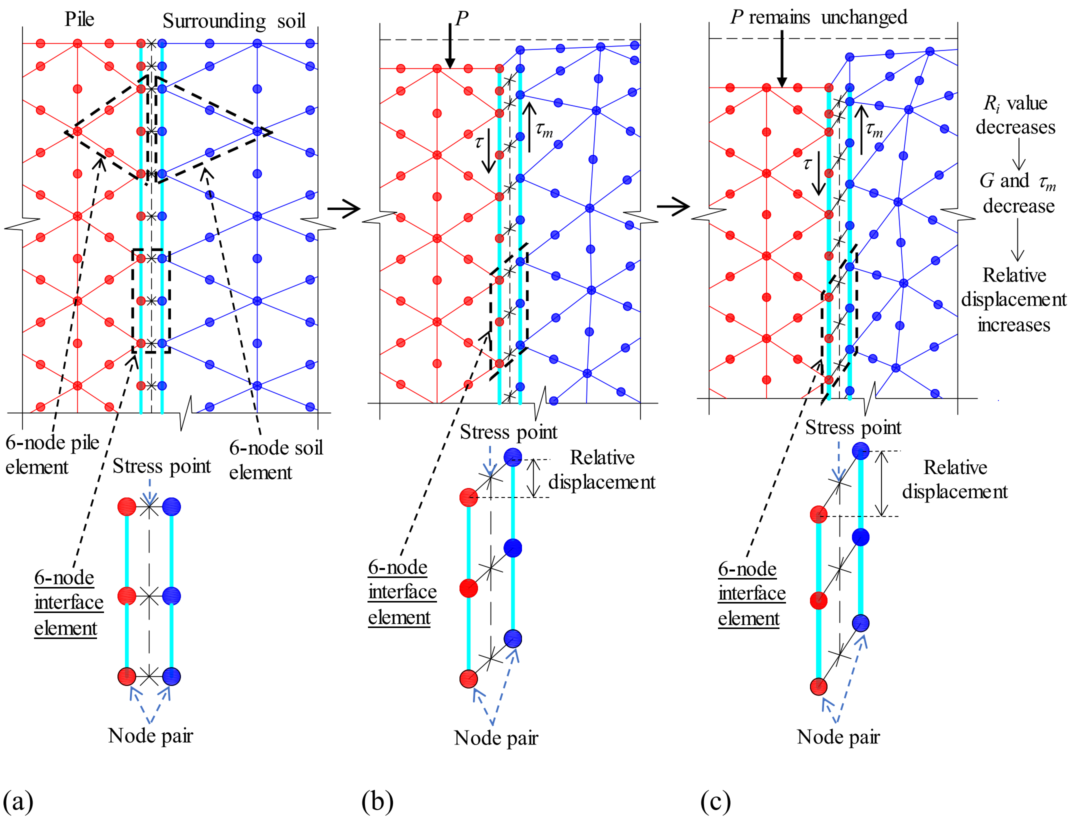

Fig. 8. Meshing diagram of pile-soil interaction using interface elements: (a) No loading on pile head; (b) Loading on pile head; (c) Reducing the R-inter value.

where $d\tau$ and $d\varepsilon$ are the incremental shear stress and shear strain of the interface, respectively; while G is the interface's shear modulus and relates to the shear modulus G_s of the soil in contact via the reduction factor R_i by the following expression:

$$G = (R_i)^2.G_s \tag{3}$$

The shear strain can then be drawn as follows:

$$d\varepsilon = \frac{d\tau}{G} = \frac{d\tau}{(R_i)^2.G_s} \tag{4}$$

This shows that behaviour of shear strain of the interface or the relative displacement between soil and pile is contingent on the value of R_i. Hence, when the R_i is small, the relative displacement between the pile and soil is large and the pile is prone to slip relative to the soil (Fig. 8c). On the other hand, when R_i is large, the bond between soil and pile is tight that does not allow significant relative displacement. The value of R_i is in the range [0–1]; appropriate selection of R_i value plays a decisive role in load-transfer behaviour as well as the shared load bearing between shaft and tip resistances that are simulated through FE modelling.

The Coulomb criterion is used to distinguish between elastic behaviour, where small displacements can occur within the interface, and plastic interface behaviour when permanent slip occurs. The elastic and plastic conditions of the interface defined based on the comparison between the shear stress (τ) and the interface's mobilised shear strength (τ_m) are described in Eq. (5) and Eq. (6), respectively.

$$|\tau| < \tau_m = \sigma_3.\tan(\varphi_i) + c_i \tag{5}$$

$$|\tau| = \tau_m = \sigma_3.\tan(\varphi_i) + c_i \tag{6}$$

where φ_i and c_i are the friction angle and cohesion of the interface, respectively. They are calculated from the associated soil strength properties (φ soil friction angle, c soil cohesion) and R_i by applying the following rules:

$$\tan(\varphi_i) = R_i.\tan(\varphi) \tag{7}$$

$$c_i = R_i.c \tag{8}$$

From Eqs. (7) and (8), the interface's mobilised shear strength can be obtained as follows:

$$\tau_m = R_i[\sigma_3.\tan(\varphi) + c] \tag{9}$$

The pile-soil interaction along the pile shaft can be described using the tri-linear softening model (Liu et al. 2004; Sharo et al. 2022) which depicts the relationship between the transfer of compression load (shear stress) at the pile-soil boundary and the relative pile shaft-soil displacement (shear displacement) as illustrated in Fig. 9. This relationship under the load can be categorized into three regimes, i.e., elastic, softening and debonding stages, in which the interface's shear stress in each step is determined by Eq. (10).

$$\tau(u) = \begin{cases} \frac{\tau_f}{u_1}u \; ; \; 0 \le u \le u_1 & (a) \\ \frac{\tau_r(u-u_1)+\tau_f(u_2-u)}{u_2-u_1} ; \; u_1 < u < u_2 & (b) \\ \tau_r ; \; u \ge u_2 & (c) \end{cases} \tag{10}$$

where; $\tau(u)$ the shear stress of the pile-soil interface; τ_f and u_1 the ultimate shear strength and corresponding shear displacement of the interface; τ_r and u_2 – the residual shear strength and corresponding shear displacement of the interface.

For very long piles as investigated in the current study ($L > 70$ m), there are multiple soil layers with different properties and considerable variation in relative soil-pile displacement along the depth. This caused significant challenges in selecting appropriate values of R_i to ensure good agreement between the numerical and field data for all points along the depth. A calibration strategy combining multiple-soil layers and –loading stages was developed to handle this issue as described in Fig. 10. In this dynamic approach, the value of R_i was changed at various soil layers and loading stages until the best fit between the numerical and field test data was achieved across all soil layers. For example, Fig. 10 shows 3 segments, i.e., S1, S2 and S3 and the average value of R_i in each segment. The development of R_i and the corresponding mobilised unit skin friction (q_s) obtained in numerical predictions changed with different loading stages. For initial loading stages, R_i was larger at the upper parts, but this order changed over the depth when the load increased, representing the yielding and debonding stages that occurred gradually from the top, thus transferring the load downward.

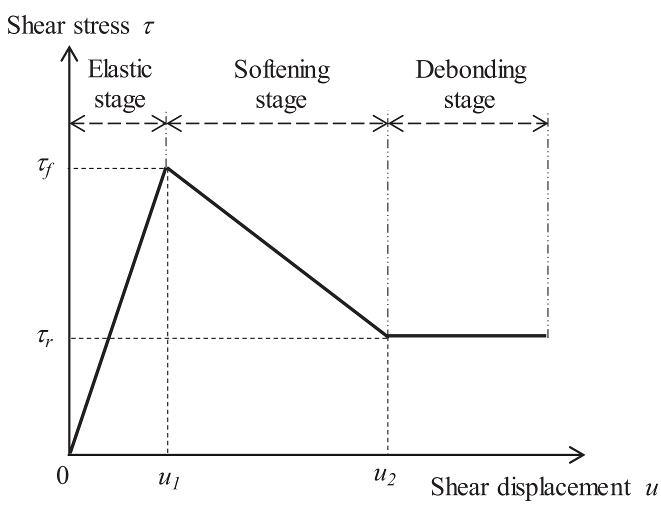

Fig. 9. Tri-linear softening shear model of the pile-soil interface.

3.3. 3D-finite element (FE) model

Boundaries of the soil-pile modelling unit were chosen to be adequately large to eliminate the boundary effects, i.e., 20x20m wide and 90 m deep. Approximately, 19,000 of 6-node triangle elements were used consistently across different cases. Meshing and defining construction phases of Pile GP are represented in Fig. 11a-b as an example of the 3D-FE modelling. The outer boundaries of the mesh were fixed against the displacements. The loading procedure was divided into three stages, including Stage 1: initial stress, Stage 2: pile installation, and Stage 3: loading. The numerical simulation process is summarized in Fig. 12. The R_i factor was calibrated through a series of iterative steps (trial and error) to ensure the discrepancy of the unit skin frictions obtained from the 3D-FE model and test data was always less than 10 %.

After completing the simulation, the R_i values versus the depth at the middle of soil layers across 4 different test piles were collated as shown in Fig. 13. Generally, the R_i has a wide distribution and tends to decrease with depth. To be specific, the R_i typically ranges from 0.4 to 0.95 for a depth within the first 10 m where weak soil layers are located, whereas it lies in a smaller range between 0.15 and 0.5

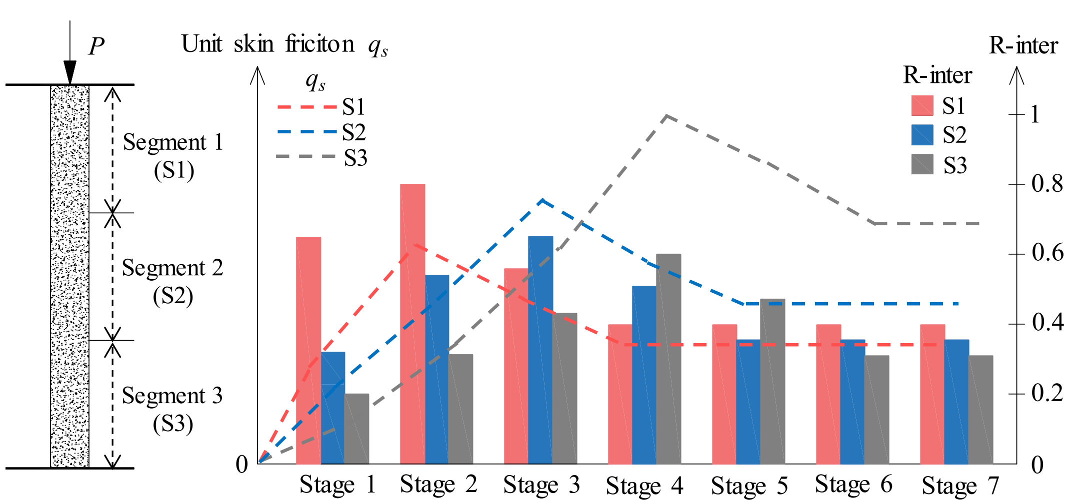

Fig. 10. Development of R-inter (R_i) and unit skin friction along 3 segments of the pile through progressive calibration process in FEM simulations.

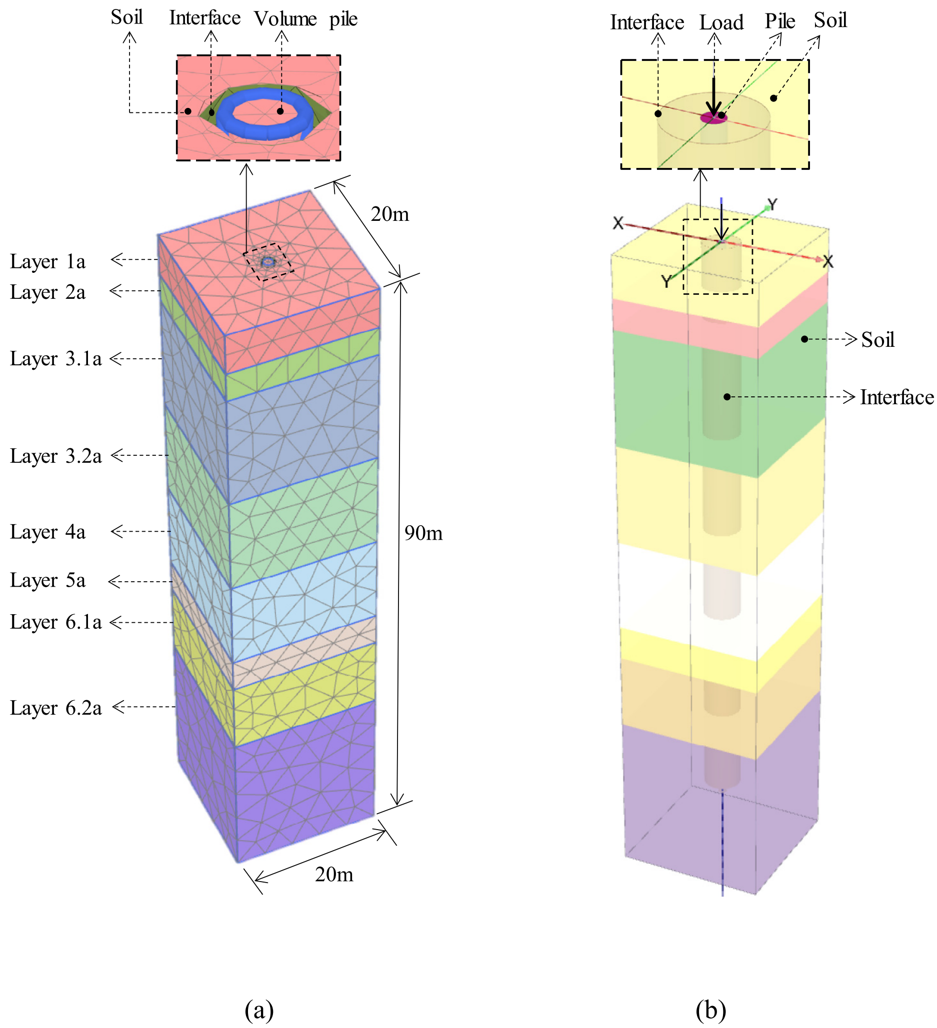

Fig. 11. 3D-FE model of Pile GP (representative case): (a) Meshing; (b) Creating construction phases (activating pile, interface elements and load).

for a depth beneath 30 m where stiffer soils are situated. Meanwhile, for a depth between 10 to 30 m, the R_i fluctuates between 0.25 and 0.65.

3.4. Verification of 3D-FE model results

In order to validate the 3D-FE models, the simulated outcomes were compared with the field test data. Firstly, developments of the unit skin friction with increasing load obtained from the simulations and field tests are presented in Fig. 14. As the figure shows, the simulated outcomes align very well with the measured data, proving concrete evidence to the effective approach and rigorous numerical modelling used in this study. It is important to note that unlike past studies where only the load–displacement behaviour at the pile head is considered, the current study enabled a comprehensive prediction to be obtained, covering the entire soil layers and loading stages. The load distributions along the pile shaft captured through FE simulations and field test data are shown in Fig. 15. In comparison with the field test data, the simulations accurately depict the process of load distribution along the pile length, with the differences in load between the simulation outcomes and experimental data at any depth consistently remaining below 8 %. Compared to other common methods such as using practice codes and empirical equations (Nguyen et al. 2024), this error threshold is considerably smaller. It is noteworthy that using constant value of R_i over different zones and loads resulted in very poor agreement with the field data, which in fact corroborated past findings (Krasiński and Wiszniewski 2017). This is understandable as R_i represents the stiffness of contact between soil and pile that heavily depends on loading and soil conditions. Those specific numerical results are not included in this paper to avoid confusion with the main results obtained from the proposed dynamic approach for R_i.

The developments of base resistance with increasing pressure and pile head displacement obtained from simulations are compared with the field test data, as shown in Fig. 16. The simulated curves nearly coincide with the measured data, attesting to the high accuracy of the developed 3D-FE models. While the base resistance in the failure piles

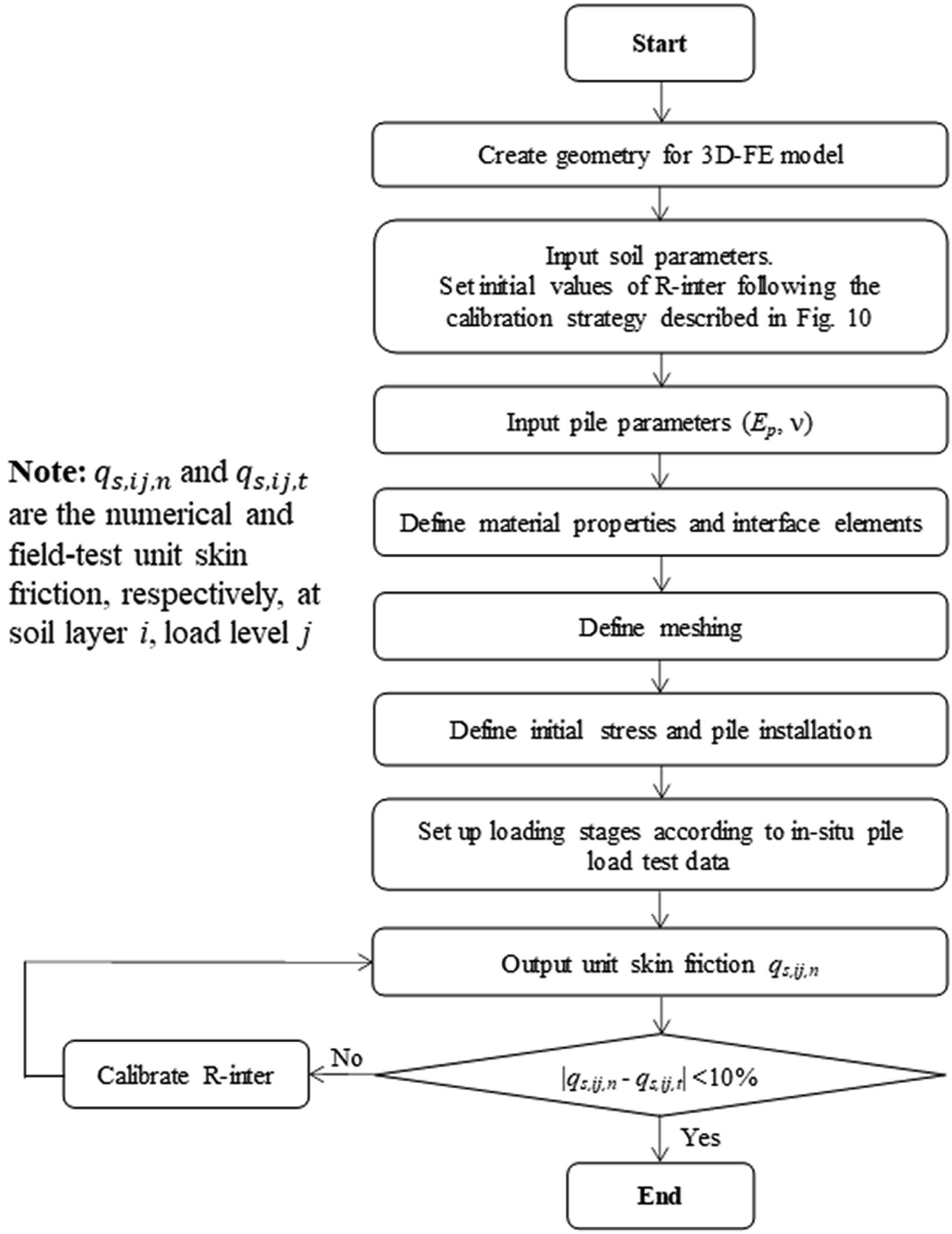

Fig. 12. Flow chart for implementation of numerical simulation process.

(Pile GP, VT and AP) experiences a sharp increase when the load pressure exceeds a certain threshold, the base resistance for the non-failure pile (Pile FT) shows a steady increase throughout the loading process. Furthermore, the results show considerable effect of pile length on the behaviour of base resistance, which is not often captured in past studies of short and medium piles. For example, both the two 70 m long piles have identical response of base resistance to increasing load pressure, however, these curves are different from those obtained in the two other 80 m long piles. For the relationship between base resistance and pile head displacement, however, the simulations overestimate the displacement measured in the field tests, as represented in Fig. 16. This was probably because the current models do not consider the pile installation effect which might have compressed the surrounding surface soil and thereby minimised the relative pile-soil settlement measured during the loading process.

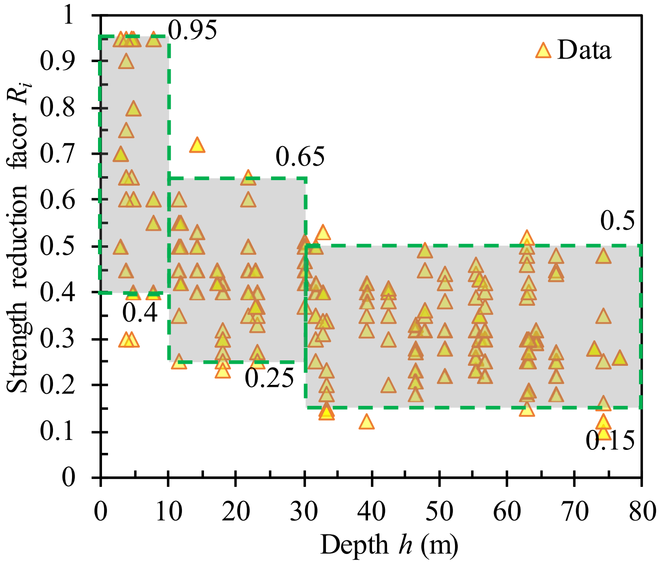

Fig. 13. Distribution of the R-inter (R_i) value according to depth.

4. Insights into load transfer process capturing mobilised skin friction and base resistance

To understand how skin friction developed with depth during loading process, the unit skin frictions obtained from field test data in the middle of each zone are plotted in Fig. 17. For failure piles (Pile GP, VT, and AP), the pile shaft-soil interaction in most of the zones reached the softening and debonding stages as the mobilised unit skin friction had decreased after reaching the peak values, except the deepest zones (e.g., Zone 7a, 7c and 7d) where the unit skin friction remained almost unchanged at the final load level (Fig. 17a, c, and d). On the contrary, for non-failure Pile FT, the soils adjacent to the pile are still in elastic stage with constant increase in skin friction until the final load level despite different depths, from Zone 2b to Zone 9b, as shown Fig. 17b. In addition, for the soft soil within 0–10 m depth in Zone 1a (Pile GP) and Zone 1d (Pile AP), skin friction mobilised very quickly to hit the highest value after the first three or four load levels. This explains why

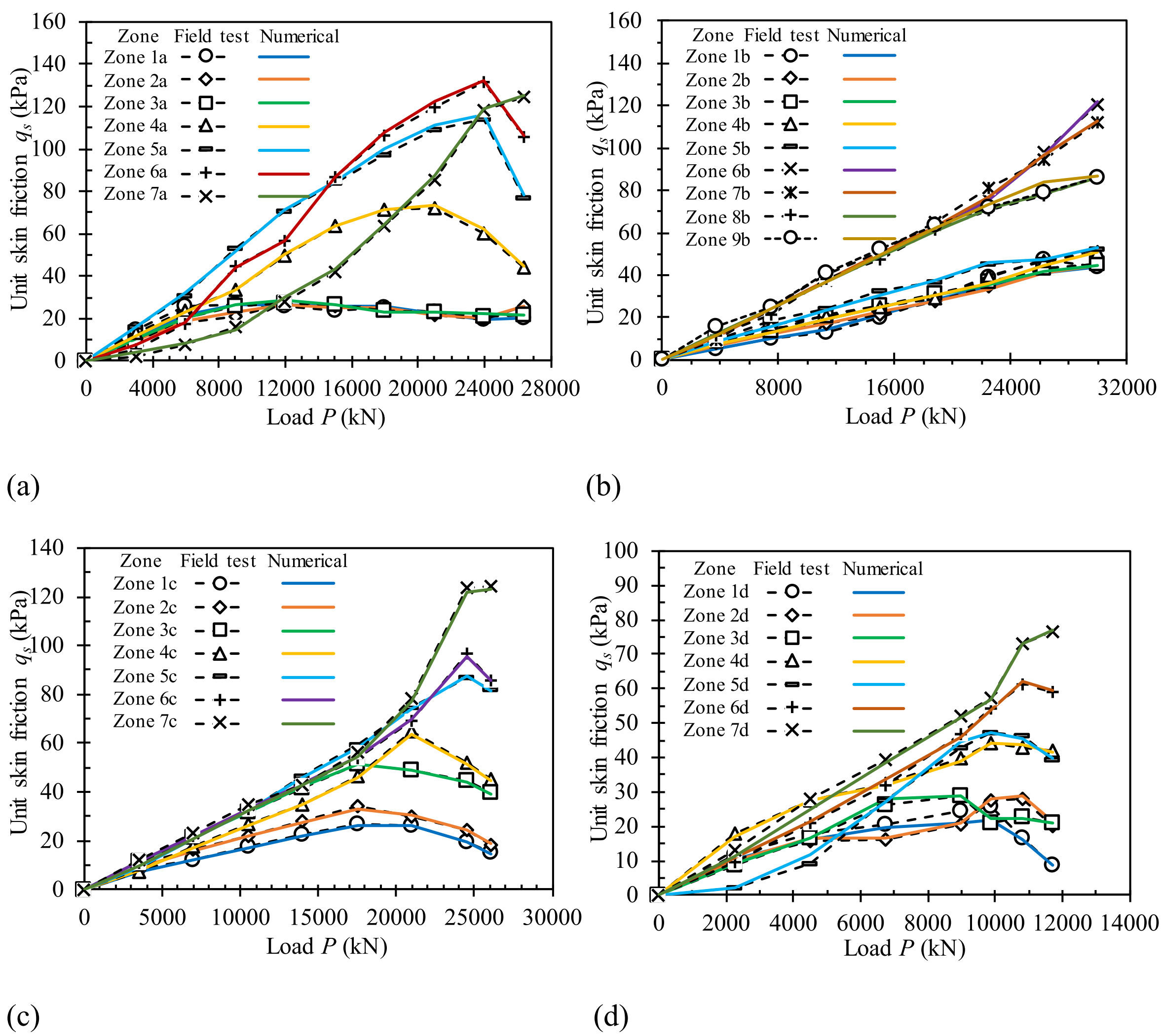

Fig. 14. Comparison of simulated and mesuared data for unit skin friction with increasing load in the 4 test piles: (a) Pile GP; (b) Pile FT; (c) Pile VT; (d) Pile AP.

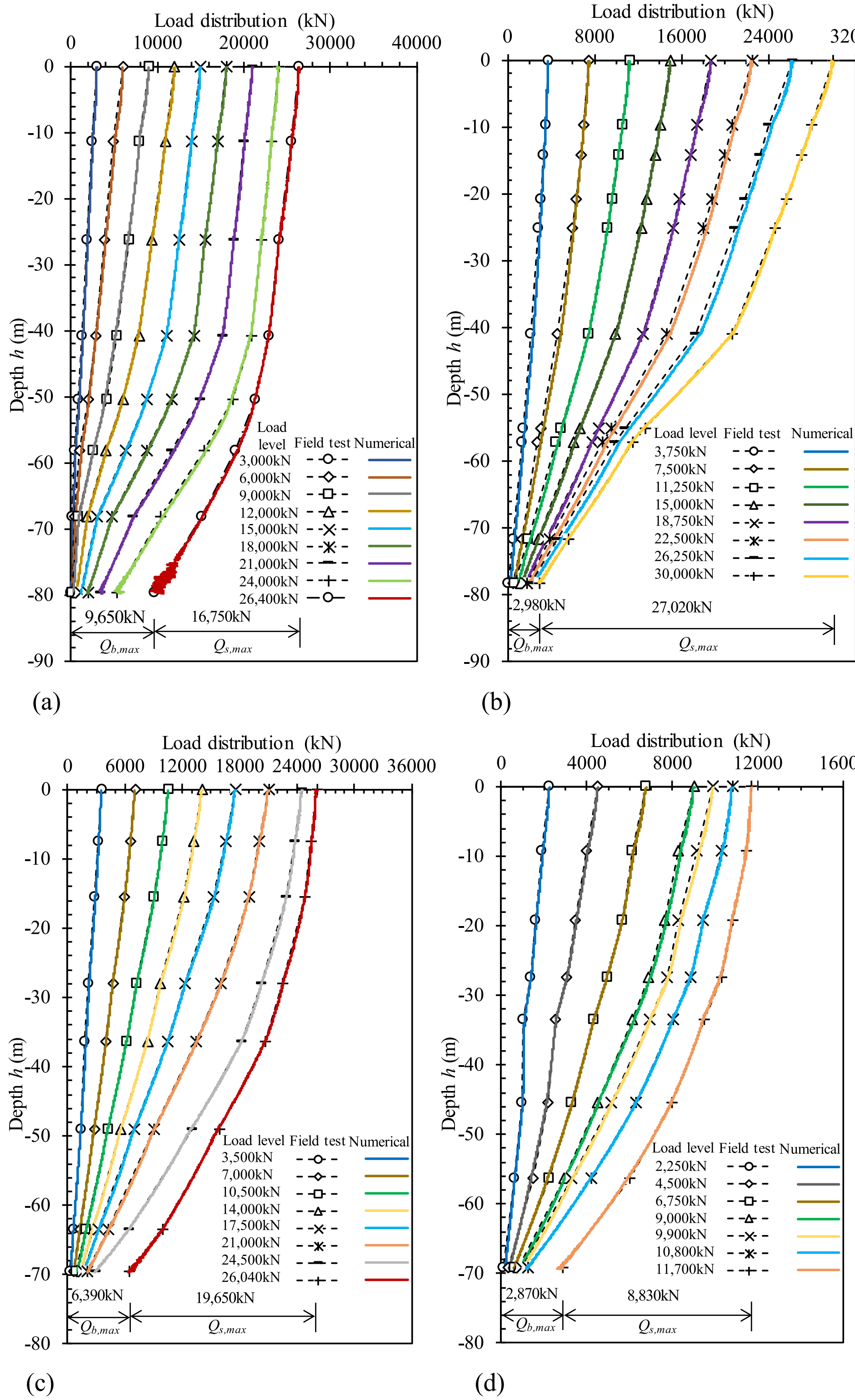

Fig. 15. Load distribution along the pile length with increasing load from field tests and simulations: (a) Pile GP; (b) Pile FT; (c) Pile VT; (d) Pile AP.

the R_i value at these zones was very high (0.8–0.95) at the initial stages before swiftly decreasing due to the degradation of the skin friction.

Fig. 17 also shows that the skin friction in deeper zones requires a larger load to reach its maximum level, which was because of the stiffer soil and higher effective stress at lower zones, plus the larger relative displacement between the top pile and the surrounding soil compared to the lower parts. This means that the maximum unit skin friction values in different zones do not occur concurrently under the

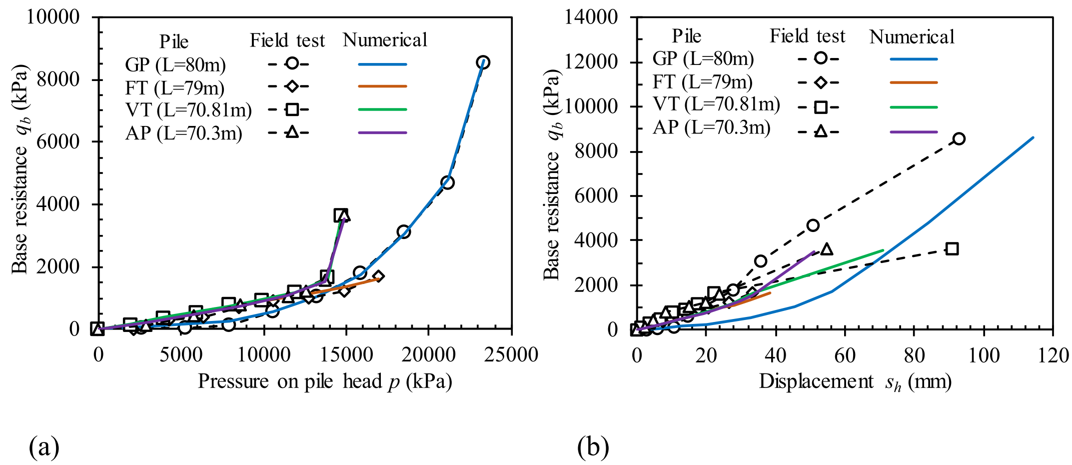

Fig. 16. Development of base resistance estimated by numerical simulations and field test data with: (a) increasing pressure at pile head; (b) increasing displacement of pile head.

same load level. As the load increases, the depth at which the maximum unit skin friction occurs shifts downward. Besides, these maximum values increase with the depth, except the non-failure Pile FT where the skin friction in Zone 6b to Zone 9b constantly develops even after ending the loading process. By connecting the maximum values of unit skin friction in all different zones, represented by the bold red line in Fig. 17, an area (i.e., the red-crossed region) of maximum skin friction along the pile shaft is generated. This, however, excludes the non-failure Pile FT (Fig. 17b) where the pile test was terminated before the failure stage (i.e., onset of maximum skin friction). On the other hand, it is important note that the active skin friction at a specific load level can be smaller than the maximum value; for example, when the upper zones fall into debonding stage (residual skin friction) while the lower parts are approaching the maximum level. In Fig. 17, the blue-crossed regions represent the active skin friction for a load of 15,000, 22,500, 21,000, and 9,900kN for Piles GP, FT, VT, and AP, respectively, corresponding to nearly the same pressure 12,000–13,000 kPa on the pile head. Under this pressure, while the unit skin frictions in the upper zones (h < 35 m) for failure Piles GP, VT, and AP (Fig. 17a, c, and d) are decreasing, the values for Pile FT (Fig. 17b) continue to grow slightly. This was because of the stiffer soils in the upper zones around Pile FT (i.e., N = 11–20 for 2 m < h < 20 m), compared to those in the other piles, as shown by the SPT values in Fig. 3. In all cases, the active region (blue) positions well within the maximum values (red line) as Fig. 17 shows.

To deepen our understanding of skin friction mobilisation under loading, the percentage of active skin friction relative to maximum skin friction, i.e., the ratio of active skin friction was calculated over different loading stages, as illustrated in Fig. 18 with 5 zones along the pile that are used for demonstration. The progression of this ratio with increasing pressure on the pile head (p) for the four tested piles is shown in Fig. 19. The results show that the ratio of active skin friction continuously rises with increasing pressure (load) until the pile reaches the critical state. Specifically, this ratio increases to a peak of around 94 % the maximum value for the three failure piles (Pile GP, VT and AP) before declining as the debonding (slip) of soil-pile contact begins to extend excessively downward. In contrast, for Pile FT, the active skin friction increases constantly and reaches the peak at the final loading stage without failure since the soil-pile contact (Zone 2b-9b) had not reached the yielding state yet. It is worth noting that the ratio of active skin friction for Pile FT was estimated using the largest value of skin friction at the final loading stage (Fig. 19) because the test was terminated before the failure. One might expect that the curve of this ratio for Pile FT would be closer to that for Pile GP if the maximum value of skin friction at failure could be used.

It is interesting that the shorter the pile, the faster the mobilisation of skin friction given the same pressure acting on the pile head. As seen in Fig. 19, the ratio of active skin friction for the 80-metre piles develops more slowly than that for the shorter ones (Pile VT and AP). This disparity becomes more pronounced at higher pressures, while the progression of the active skin friction ratio for the two shorter piles (L = 70 m) is almost identical throughout the loading. The tendency that this ratio develops with increasing pressure for the two longer piles (L = 79 and 80 m) is quite similar, despite having different peak points due to different conditions of test termination as explained earlier. This indicates that the ratio of active skin friction is influenced significantly by the pile length. It is important to note that the extended length from 70 to 80 depth, despite accounting for only 14 % of the total length, was mainly within stiff soils (i.e., Layer 6a for Pile GP and Layer 9b for Pile FT, see Fig. 3). These soils have the average N value > 40, especially Layer 9b is sandy soil with SPT N > 50. This certainly added considerable skin and base resistances to the pile's bearing capacity compared to other piles where L < 71 m. For example, Fig. 20b shows

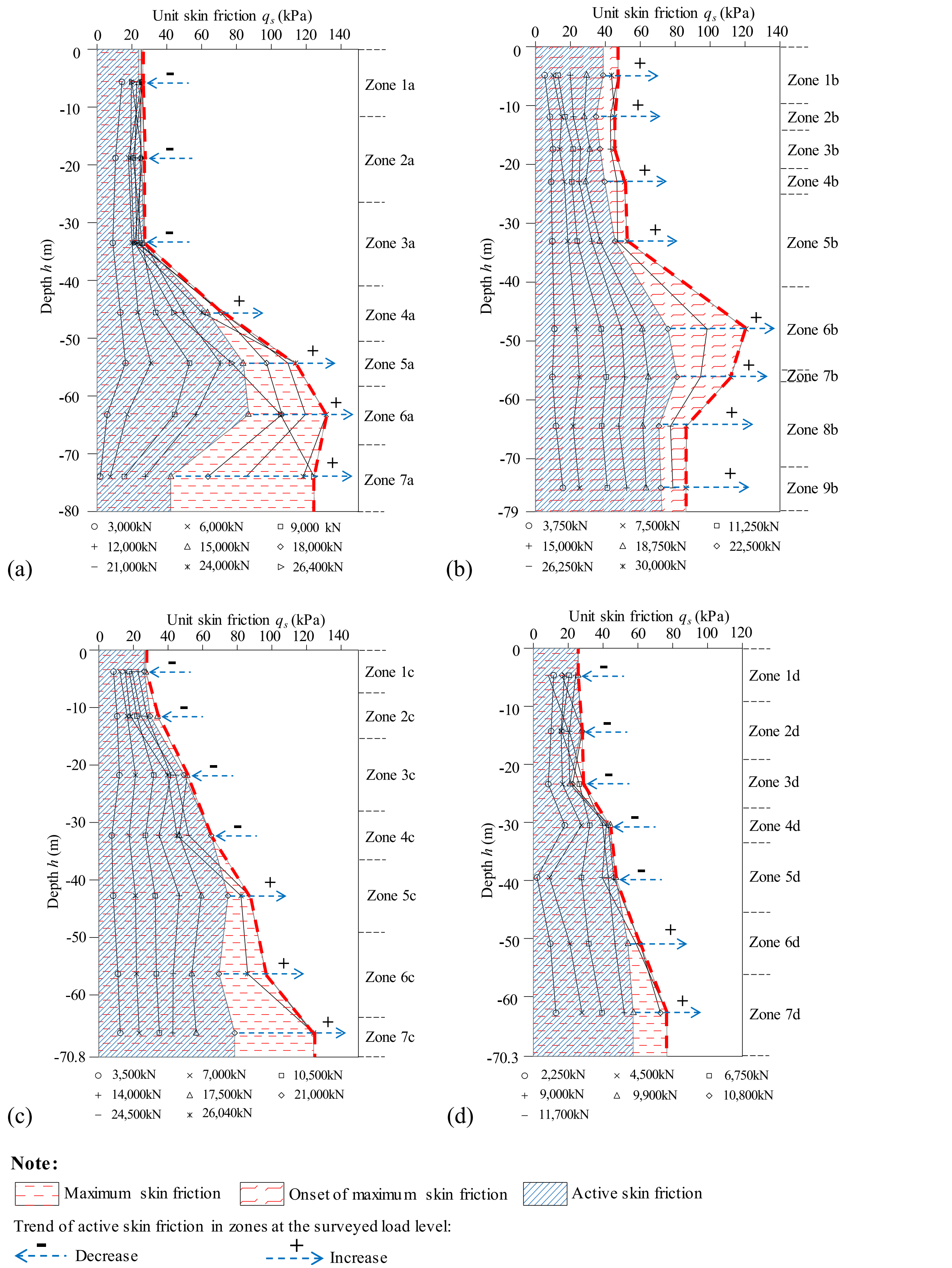

Fig. 17. Mobilisation of skin friction with depth during the loading process: (a) Pile GP; (b) Pile FT; (c) Pile VT; (d) Pile AP. Active skin friction is plotted at a representative load.

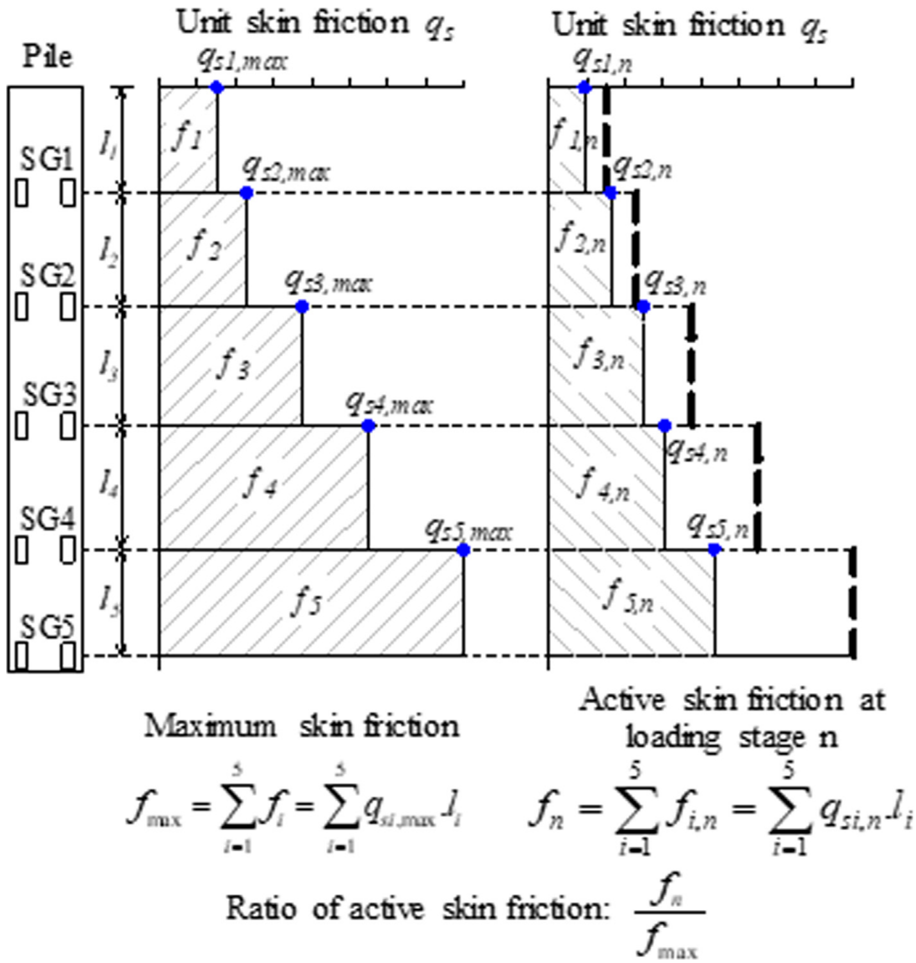

Fig. 18. Schematic diagram for determining the ratio of active skin friction.

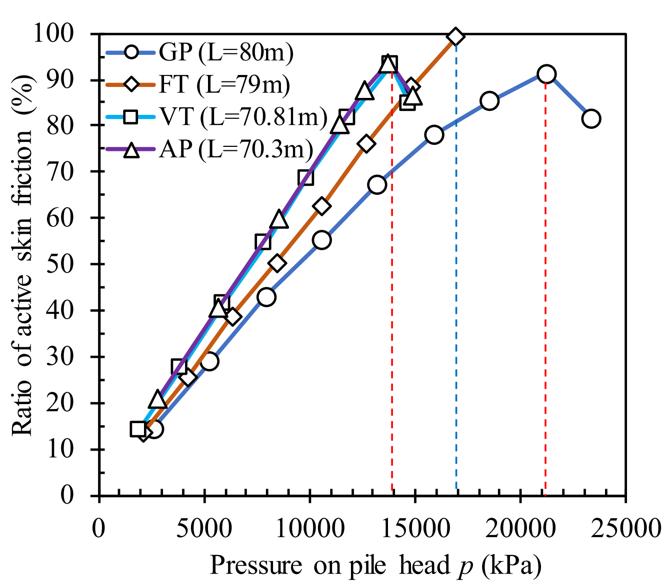

Fig. 19. Ratio of active skin friction over increasing pressure on pile head.

significantly larger base resistance of 80 m long pile (e.g., Pile GP) compared to 70 m long piles, indicating the role of soil stiffness underneath the pile toe.

To gain further insight into the load transfer behaviour, the share ratios between the skin friction (shaft) and base resistance to the total bearing capacity of the piles were computed. The base resistance usually carries a minor portion of the applied load in the initial stages and only makes a larger contribution to the total bearing capacity at the later loading stages, especially when piles begin to fail under loading (Fig. 20b). For instance, for Pile GP, the base resistance carried 9,650kN and contributed up to 37 % of the total bearing capacity at the final load level. However, compared to the skin friction, the share ratio of the base resistance to the total bearing capacity was always significantly smaller during the entire process of loading, as described in Fig. 20. This highlights that skin friction along the pile shaft is the primary contributor to the overall bearing capacity of long to super-long piles (60–100 m long) (Nguyen et al. 2024). As seen in the Fig. 20b, the base resistance accounts for 25 % to 35 % of total bearing capacity for the failure piles, but only 10 % for the non-failure pile (Pile FT) at the highest loading pressure. For failure piles, the share ratio of skin friction experiences a steady decrease before a sharp drop as the pile reached a critical state where the friction between pile and soil in the deeper zones begun to transfer from

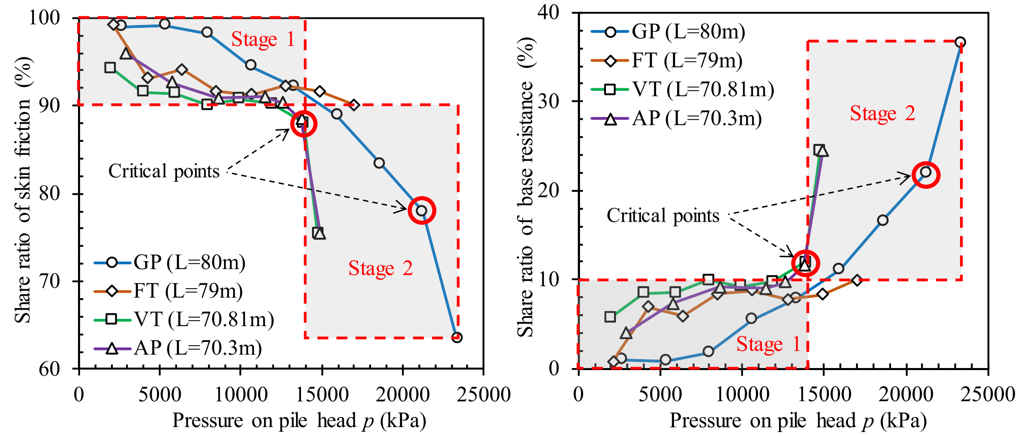

(a) (b)

Fig. 20. Share ratios of skin friction and base resistance to the total bearing capacity of the piles with increasing pressure: (a) skin friction; (b) base resistance.

the peak to the residual stage. In contrast, the share ratio of base resistance consistently rises before a swift turn at the critical point. The 70 m long piles reached the critical state at a pressure of 14,000 kPa, which was considerably smaller than that, i.e., 21,000 kPa in the 80 m long pile. At this transition point, the share ratio of base resistance was around only 10 % for the shorter piles (70 m), compared to nearly 20 % for the longer piles. The share ratio of skin friction for 80 m long piles was always larger than that for 70 m long piles under the same pressure. It can be concluded that for piles with a length ranging from 70 m to 80 m installed in soft soil of Mekong Delta, the contribution of skin friction and base resistance can be approximately divided into two distinct stages corresponding to Stage 1 and Stage 2 shown in Fig. 20. While the share ratios of skin friction and base resistance slightly decrease and increase, respectively in Stage 1, they vary swiftly when entering Stage 2. Specifically, the skin friction accounts for more than 90 % of the bearing capacity when the load pressure < 14,000 kPa, but its contribution decreases sharply to 63 % when the pressure increases to 23,500 kPa. Share ratios between skin friction and base resistance are given in conjunction with the applied pressure and displacement of the pile head in Table 3.

How the share ratios of skin friction and base resistance respond against the rise of pile head displacement (s_h) is represented in Fig. 21. The 70 m long piles reached the critical point at a displacement of roughly 25 mm, earlier than the 80 m long piles which only achieved the same state at nearly 50 mm displacement. At the critical condition, the share ratio of base resistance was around 10 % for the shorter piles and 20 % for the longer piles. Additionally, contribution from skin friction for the longer piles was consistently greater than that for the shorter piles under the same displacement. Considering the rate of increment between two loading steps, two distinct stages corresponding to Stage 1 and Stage 2 can be identified at the critical threshold of 25 mm, as depicted in Fig. 21 and Table 3. The share ratio of skin friction moderately decreases in Stage 1 (s_h < 25 mm), whereas it substantially drops in Stage 2 (s_h > 25 mm). In contrast, an opposite pattern is observed for base resistance.

5. Characterisation of R-inter (R_i) and proposed design chart

In order to facilitate the practical application of the current FE model outcomes, semi-empirical correlations between the R_i factor and other input parameters were investigated. Due to the wide variation of the R_i with different soil layers and loads, establishing relationships between the R_i and constant soil parameters would result in low confidence. As a result, the mean R-inter value ($R_{i,m}$) in a particular soil layer and key soil parameters, including the vertical effective stress at the middle of the soil layer

Table 3
Contributions of shaft friction and base resistance to the total bearing capacity of piles according to different ranges of pressure and displacement on the pile head.

Stage	Pressure on pile head, p (kPa)	Pile head displacement, s_h (mm)	Share ratio to the total bearing capcity (%)	
			Skin friction	Base resistance
Stage 1	< 14,000	< 25	> 90	< 10
Stage 2	14,000–23,500	25–93	63–90	10–37

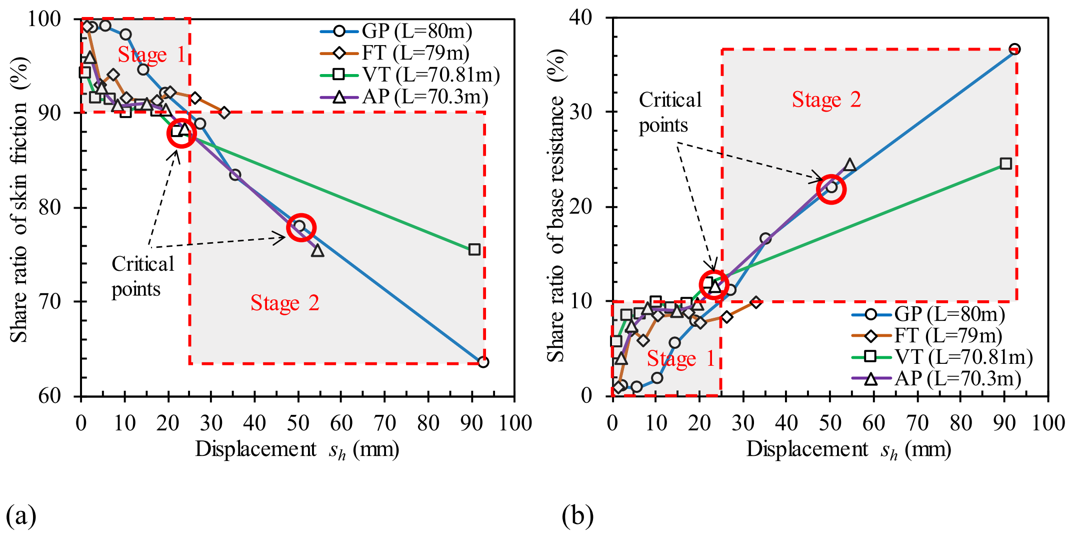

Fig. 21. Share ratio of skin friction and base resistance to the total bearing capacity of the piles with increasing displacement: (a) Skin friction; (b) Base resistance.

(σ'_1), the shear strength of soil (τ_{max}), and the average SPT value (N) were considered. Their relationships are presented in Fig. 22 with a fairly high degree of R^2 (> 0.8). Similar to its distribution with depth (as shown earlier in Fig. 13), the R_i tends to decrease as the magnitude of these soil parameters increases. In fact, the effective stress of soil shows the predominant influence on the behaviour of R_i with the most apparent trend, i.e., $R^2 = 0.893$. This is understandable as the effective stress of soil can be used effectively to represent the frictional strength between soil and pile according to Coulomb's theory. Exponential function is adopted to establish relationships between the R_i and these soil parameters, as presented in Eq. (11), (12), and (13). Although these equations do not capture the variation of the R_i in every soil layer, they provide a representative mean value of R_i for each soil layer based on its fundamental parameters, enabling design engineers to select appropriate values of R_i for an acceptable FE modelling.

$$R_{i,m} = 2.354(\sigma'_1)^{-0.312} \tag{11}$$

$$R_{i,m} = 2.409(\tau_{\max})^{-0.385} \tag{12}$$

$$R_{i,m} = 1.06N^{-0.337} \tag{13}$$

As shown in earlier finding, R_i value can vary within a specific soil layer as the load increases, the load has a significant influence on the magnitude of R_i, in addition to the soil properties. Hence, the relationships between the R_i and input parameters consisting of load and soil parameters was proposed based on numerical results as follows:

$$R_i = 0.523\left(\frac{p}{\tau_{\max}.\sigma'_1}\right)^{0.21} \tag{14}$$

The results (Fig. 23) show a good agreement ($R^2 = 0.81$) between the R_i and 3 input parameters, i.e., the pressure on the pile head (p), shear strength and effective stress of soil, as depicted by Eq. (14). Additionally, since the variation of R_i was found to have an immediate impact on the magnitude of mobilised skin friction for a given soil layer, an exponential function describing the relationship between the R_i and normalised unit skin friction was implemented, as represented in Eq. (15) as follows.

$$R_i = 2.313\left(\frac{k_s}{\sigma'_1}\right)^{0.256} \tag{15}$$

where $k_s = \frac{q_s}{\tau_{\max}}$ – normalised mobilised skin friction; q_s unit skin friction (kPa).

Fig. 24 shows that the proposed relationship in Eq. (15) provides a higher R^2 value (0.87) compared to that yielded from Eq. (14), attesting to the direct influence of the mobilised skin friction between soil and pile on the R_i value. However, the major advantage of Eq. (14) is the use of easy-to-determine parameters, i.e., loading pressure, the effective stress and shear strength of soil, whereas the skin friction q_s in Eq. (15) might require more complex tests and calculations to gain sufficient confidence. Neverthelss, these 2 equations can be combined effectively to obtain possible values of R_i, facilitating fast and accurate modelling. In short, these simple empirical equations offer a swift approach for practical engineers to conveniently estimate the values of the R_i for finite element modelling of long piles in multi-layer soft soil adopting fundamental soil parameters, i.e., the effective stress and shear strength, and the applied load pressure on the pile.

In general, in addition to significantly reducing the cost of estimating the ultimate bearing capacity of piles based on the static load tests, as outlined in various foundation design codes (Eurocode 1997–1 2004; Mohurd 2011), the FE modelling provides a more insightful understanding of the mobilised skin friction and base resistance in pile-soil interaction under loading. Conventional methods which are commonly used in practice to estimate ultimate

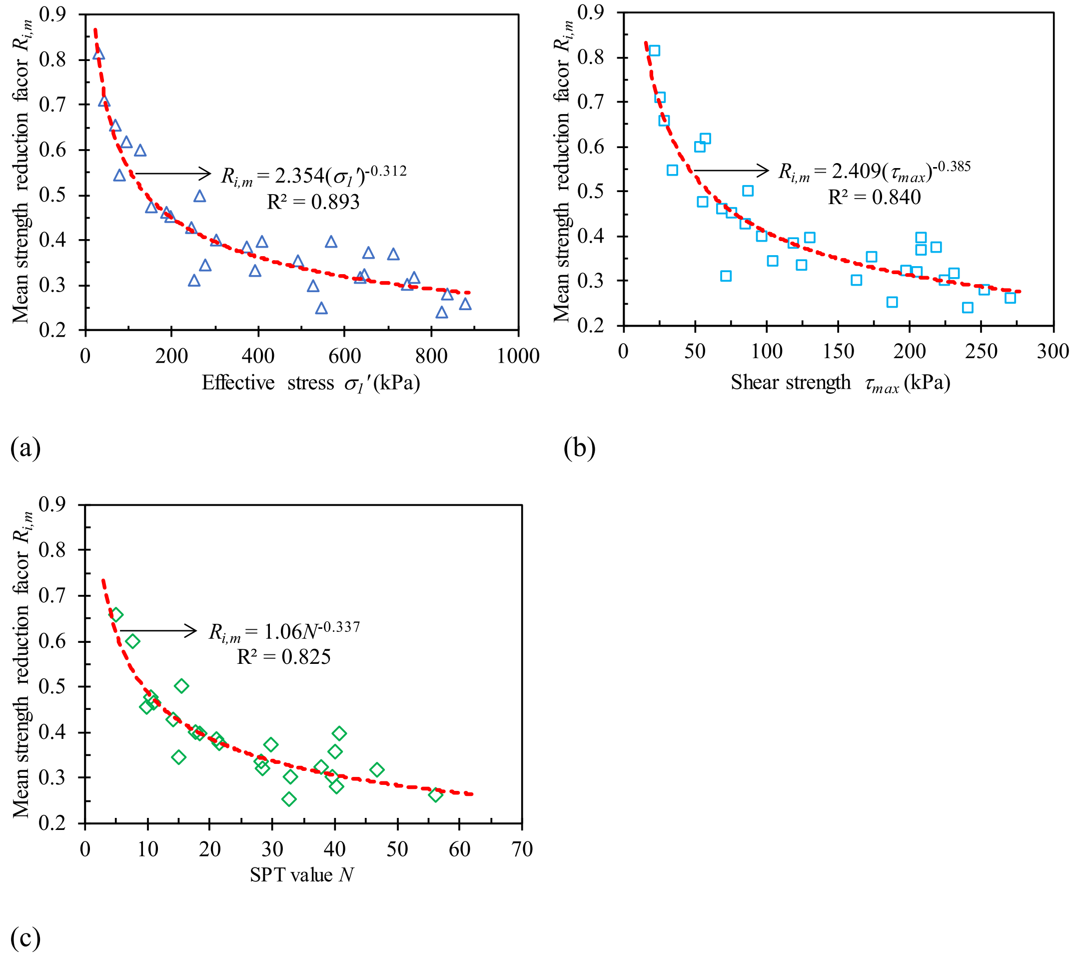

Fig. 22. Mean R-inter (R_i) versus soil parameters: (a) effective stress; (b) shear strength; (c) SPT value.

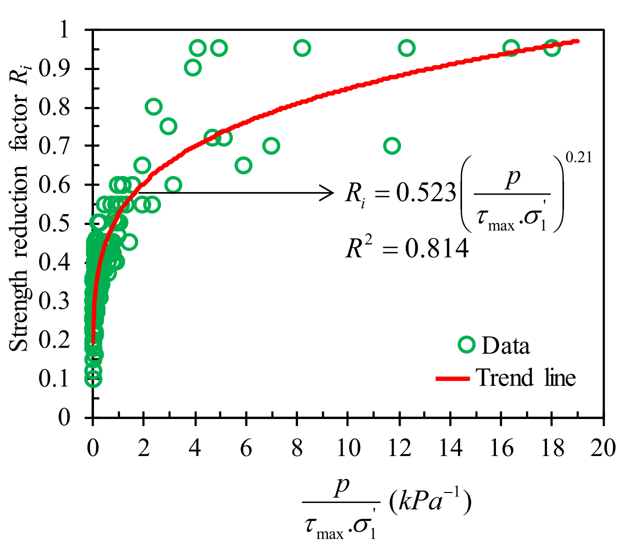

Fig. 23. Relationship between the R_i and the applied load pressure and effective stress of soil.

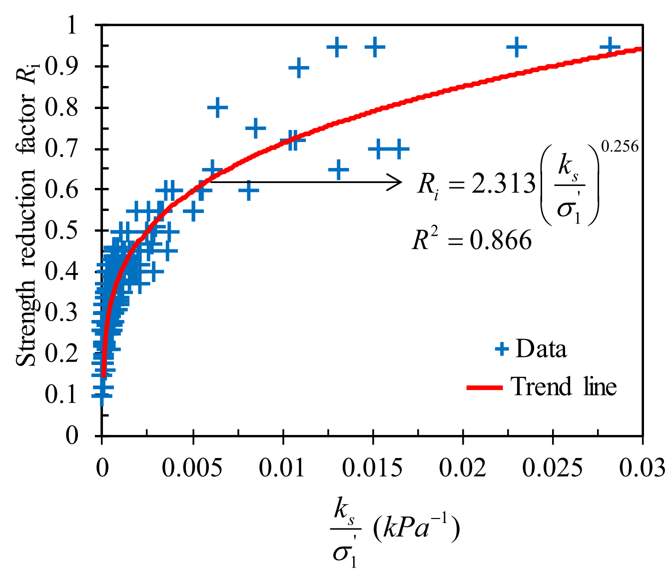

Fig. 24. Relationship between the R_i and normalised unit skin friction.

bearing capacity of piles, such as the use of SPT values (AASHTO Specifications 2010; Decourt 1995; Meyerhof George 1976; TCVN 10304 2014) and cone penetration tests (CPT) (Eslami and Fellenius 1997; Eurocode 1997–1 2004; Schmertmann 1978; TCVN 10304 2014) are often reported to cause significant deviation from the actual values measured in pile tests. The proposed equations to estimate the R-inter value would promote finite element method FEM in practical design of deep pile foundation by reducing computational costs while enhancing the accuracy and confidence of prediction.

6. Validation of the proposed method to calculate R-inter (R_i)

In this section, a large and long bored pile ($D = 0.956$ m and $L = 58.3$ m), namely PFJ1, installed in Shanghai soft soil strata (Liu et al. 2017) is employed to validate the applicability of the proposed method to calculate the R_i in practice. It is important to note that despite various attempts by the authors, it was very challenging to obtain reliable and sufficient field test data from independent studies for large and long bored piles in soft soil. Geological condition of the PFJ1 pile is characterised by alternating layers of clay and sand as portrayed in Fig. 25. In order to determine shaft and base resistances of the pile, strain gauges were installed along the pile shaft and at soil layer interfaces and adjacent to the pile tip, as shown in Fig. 25. The current study divided the soil profile into 9 different layers according to the soil type and position of strain gauges for convenient calculation. Soil parameters used for the current modelling (Hardening Soil HS model) were taken from previous study with reference to laboratory test report (Liu et al. 2017), as summarised in Table 4. These soil parameters are relatively relevant to those in Mekong Delta that were investigated earlier in this paper (Table 2). The values of the R_i were calculated using Eq. (14) based on the pressure applied on the pile head (p), effective stress (σ'_1), and shear strength (τ_{max}) of soils. For example, for Layer A, the first applied pressure level (2,229 kPa) was determined at a load of 1600 kN, and σ'_1 and $\tau_{max} = 57$ kPa and 18.3 kPa were calculated at the middle of the layer, resulting in $R_i = 0.61$. Similar calculations were made to determine the values of R_i for different soil layers and loading levels.

The simulated outcomes, including the unit skin friction at different layers and the load distribution over the depth, are shown in Fig. 26 in comparison with the field data. The results show good agreements between the predicted and the measured data. The estimated unit skin friction is relatively well aligned with the measured data for most soil layers, for example Layer A, B, D, E and F have the largest deviation < 10 %. The exception only occurs to Layer C which is considerably thinner than other layers, the disparity for this case reaches 20 %. It is noteworthy that the prediction result of Layer H is not included in this comparison because this layer has very small contact area with the pile shaft (see Fig. 25), making the field measurement data unavailable for validation. Fig. 26c represents the load distribution over the depth for different loading levels from 1,600 to 6,800kN. Apparently, the simulated results match the experimental data quite well, especially for the

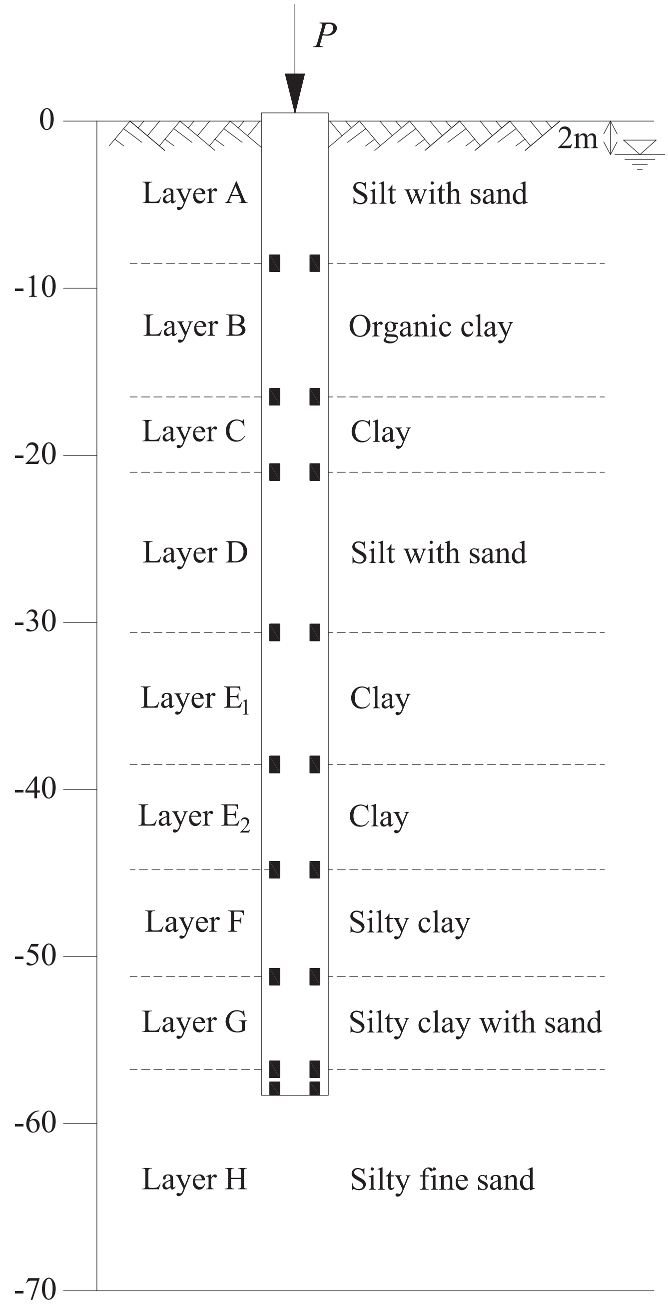

Fig. 25. Soil profile of the test pile PFJ1 used for validation, data extracted from field study by Liu et al. (2017).

$h < 20$ m. The deviation becomes larger when the load is bigger, however, this is certainly acceptable when compared to conventional methods such as using design codes and empirical equations that are commonly used in practice (AASHTO Specifications 2010; Nguyen et al. 2024). Overall, the proposed method to calculate R_i has shown significant success in enhancing the accuracy of FE simulation for long and large piles installed in soft soil, demonstrating great potential for advancing practical design.

On the other hand, based on Eq. (15), unit skin friction of a soil-pile segment can be back calculated by Eq. (16)

Table 4
Input parameters of soil layers using Hardening Soil (HS) model in validation pile

Layer	Depth, h (m)	γ (kN/m^3)	e	φ' (deg)	c' (kPa)	E_{50}^{ref}(kPa)	m
A	0–8.5	18.6	0.86	29	2	10,500	0.55
B	8.5–16.5	16.1	1.34	25	15	15,500	0.9
C	16.5–21	17.1	1.3	28	26	22,600	0.75
D	21–30.6	18	1.03	29	2	25,800	0.55
E_1	30.6–38.5	18.2	0.94	28.5	22	31,000	0.75
E_2	38.5–44.8	18.2	0.94	28.5	22	35,560	0.75
F	44.8–51.2	17.9	1.01	28	18	38,800	0.75
G	51.2–56.8	18.2	0.94	30	10	49,000	0.55
H	56.8–70	18.6	0.78	31	1.5	55,400	0.55

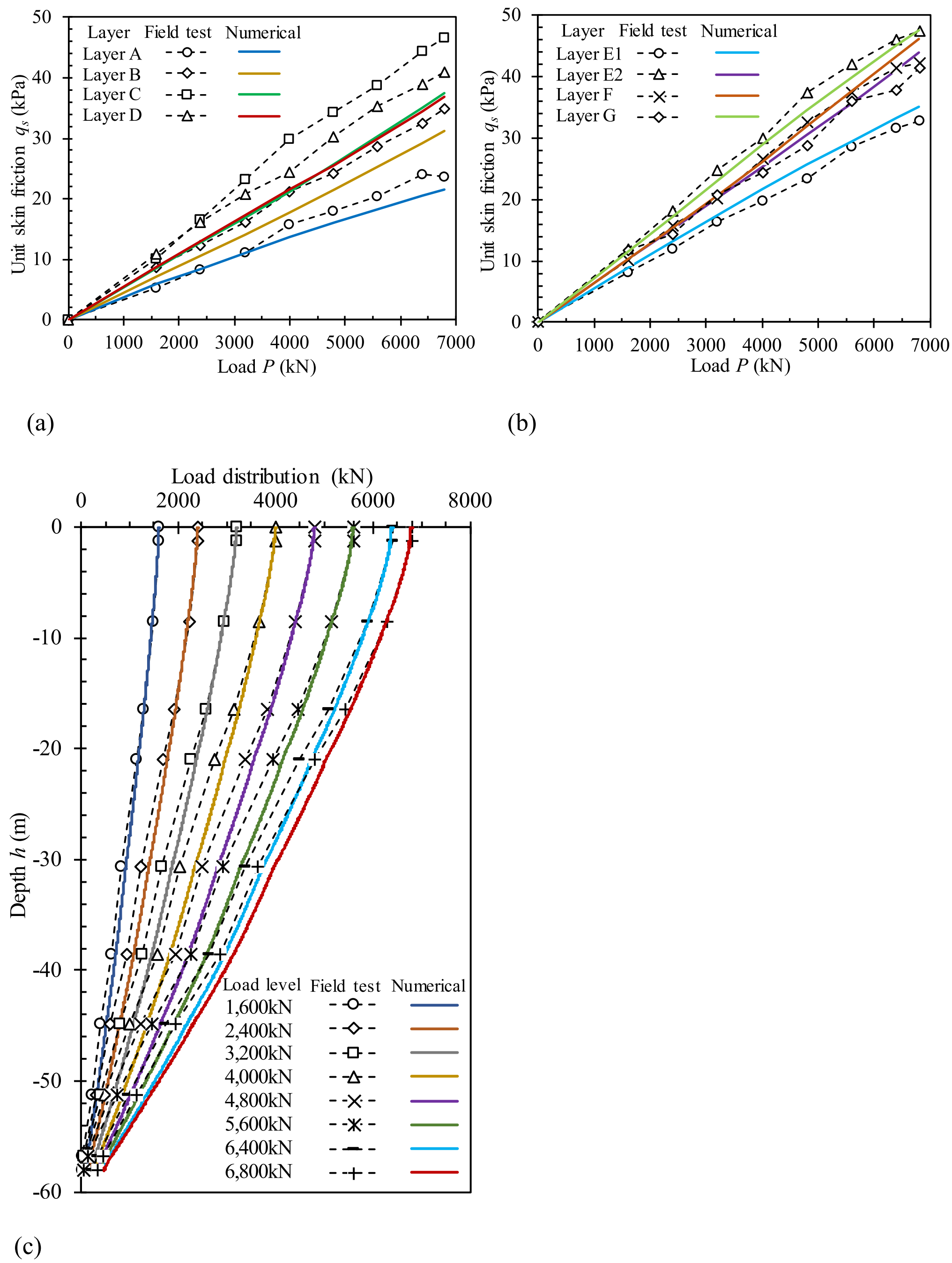

Fig. 26. Comparisons of the current simulated results and previous measured data (Liu et al. 2017): (a) Unit skin friction with increasing load for Layer A to Layer D; (b) Unit skin friction with increasing load for Layer E_1 to Layer G; (c) Load distribution along the pile length with increasing load.

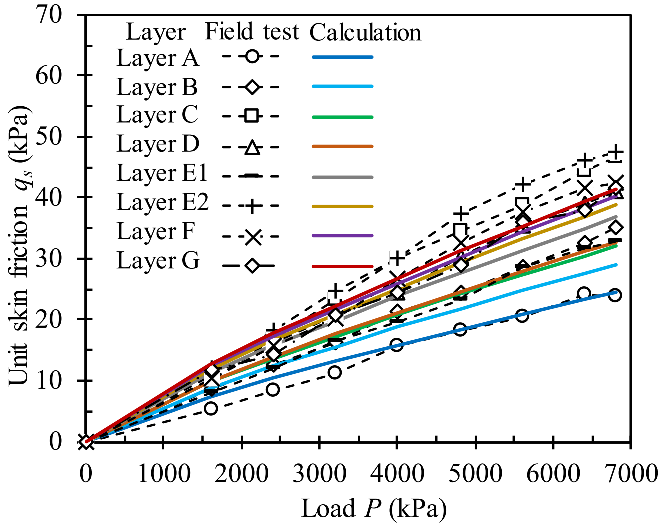

Fig. 27. Comparisons of the calculated and measured data for unit skin friction with increasing load.

with reference to the value of R_i which is determined earlier using Eq. (14). In other words, combining Eq. (14) and Eq. (16) allows one to determine the unit skin friction of pile at any particular soil layer. For example, Fig. 27 shows the unit skin friction calculated by the combination of Eq. (14) and Eq. (16) in comparison with the measured data. The results indicate that the direct calculation method can well estimate the evolution of skin friction over different depths and loads with the deviation between the calculated and measured values well under 30 %. This direct calculation method enables practical engineers to effectively estimate skin friction and the corresponding bearing capacity of pile foundation with an acceptable accuracy, giving significant value to promote the efficiency of design and construction in practice.

$$q_s = 0.038R_i^{3.91}.\sigma'_1.\tau_{\max} \tag{16}$$

7. Conclusion

The current study carried out extensive experimental (field test) and numerical investigations into the load-transfer process involving mobilised skin friction (shaft resistance) and base resistance of super-long piles (70–80 m) installed in multi-layer soft soil of Mekong Delta. Four static pile load tests with detailed instrumentation over the depth were analysed to obtain skin friction and base resistance over different loading stages. Three-dimensional finite element FE models incorporating interface elements between soil and pile were developed with the shear reduction factor R-inter (R_i) that was calibrated based on multiple-soil layer and-loading stage validation process. The results do not only show excellent agreement between the numerical and field data, but also significantly advance our understanding of soil-pile interaction and FE modelling capabilities. Salient findings from this study can be highlighted as follows.

- The developed FE models based on multiple stages of calibration successfully simulated pile load tests with high degree of accuracy. The deviation between numerical and measured skin friction across different soil layers along the pile was less than 10 % throughout the 4 different test cases. The load-transfer process, including the 3-stages progression of skin friction associated with its downward propagation over depth, was fully reproduced in tandem with rising base resistance. This led to a conclusion that using interface elements in FE modelling should be implemented with proper selection of the shear reduction factor to ensure accurate predictions, especially for the plastic regime and ultimate failure of pile foundation.
- The length of pile was found to significantly affect the ratio of active skin friction (i.e., the ratio between the current to the maximum skin friction) under loading. The shorter the pile, the faster the mobilisation of skin friction, given the same pressure acting on the pile head. Nevertheless, the entire active skin friction was found to reach around 90 % the maximum (theoretical) level before decreasing, despite different pile lengths.
- For long piles from 70 m to 80 m installed in soft soil, two major stages in load-transfer progress were defined. The first stage was marked by the displacement of pile head $s_h < 25$ mm and the pressure $p < 14{,}000$ kPa, where the skin friction took majority of bearing capacity (> 90 %). When s_h exceeds 25 mm and $p > 14{,}000$ kPa, the second stage begun with a sharp drop in skin friction (to 63 %) and a rapid increase in base resistance (reached 37 %). In this stage, soil and pile slipped over each other (debonding state) at most sections of the pile, resulting in residual skin friction with excessive rise in pile displacement.
- Through the extensive data of R_i obtained from FE modelling, the average value of R_i in a soil layer was found to decrease in a power law with increasing effective stress (σ'_1), shear strength (τ_{max}) and SPT value (N) of the soil. Combining soil properties and loading pressure, two novel equations, i.e., Eqs. (14) and (15) were proposed to calculate exact value of R_i with an acceptable prediction accuracy, $R^2 = 0.81$ and 0.87. Comparison between the FE analysis using the values of R_i obtained from these equations and the field measurement from independent studies showed a high accuracy of prediction over unit skin friction with the average error < 10 %.

Although the current study has proved significant advancement of using dynamic value of R_i in numerical FE simulation of long piles in multiple soil layers, it has not addressed the complex behaviour of soil deformation. How varying R_i over different loading stages can affect ground deformation against depth and radius would deserve considerable effort in future investigations.

CRediT authorship contribution statement

Thoi Huu Tra: Writing – original draft, Visualization, Validation, Software, Resources, Methodology, Investigation, Formal analysis, Data curation. **Thanh T. Nguyen:** Writing – review & editing, Writing – original draft, Validation, Supervision, Methodology, Funding acquisition, Formal analysis, Conceptualization. **Thien Q. Huynh:** Validation, Resources, Methodology, Data curation. **Tatsuya Ishikawa:** Writing – review & editing, Validation, Data curation.

Data availability

The data used in the current study are available from the corresponding author upon reasonable request.

Acknowledgements

This research was supported by Australian Research Council (DE230101127) and Transport Research Centre (TRC), University of Technology Sydney.

References

AASHTO Specifications. 2010. LRFD Bridge Design Specification. American Association of State Highway Officials, Washington.

Abu-Farsakh, M., Rosti, F., Souri, A., 2015. Evaluating pile installation and subsequent thixotropic and consolidation effects on setup by numerical simulation for full-scale pile load tests. Can. Geotech. J. 52 (11), 1734–1746. https://doi.org/10.1139/cgj-2014-0470.

Al-Atroush, M.E., Hefny, A., Zaghloul, Y., Sorour, T., 2020. Behavior of a large diameter bored pile in drained and undrained conditions: Comparative analysis. Geosciences 10 (7).

Alwalan, M.F., El Naggar, M.H., 2020. Finite element analysis of helical piles subjected to axial impact loading. Comput. Geotech. 123, 103597. https://doi.org/10.1016/j.compgeo.2020.103597.

Amornfa, K., Sa-nguanduan, N., 2023. Load-displacement behavior of single pile in sand using physical model test and finite element method. GEOMATE Journal 24 (103), 68–75.

ASTM D1143. 1981. Standard Test Method for Piles Under Static Axial Compressive Load. Annual Book of ASTM standards, USA.

Bentley. 2022. Plaxis 3D - Reference manual.

Decourt, L. 1995. Prediction of load settlement relationships for foundations on the basis of the SPT-T. Ciclo de Conferencias Inter. "Leonardo Zeevaert", UNAM, Mexico: 85-104.

Eslami, A., Fellenius, B.H., 1997. Pile capacity by direct CPT and CPTu methods applied to 102 case histories. Can. Geotech. J. 34 (6), 886–904. https://doi.org/10.1139/t97-056.

Eurocode 1997-1. 2004. Geotechnical Design–Part 1: General Rules. Springer London.

Galvín, P., Romero, A., Solís, M., Domínguez, J., 2017. Dynamic characterisation of wind turbine towers account for a monopile foundation and different soil conditions. Struct. Infrastruct. Eng. 13 (7), 942–954. https://doi.org/10.1080/15732479.2016.1227342.

Hamderi, M., 2018. Comprehensive group pile settlement formula based on 3D finite element analyses. Soils Found. 58 (1), 1–15. https://doi.org/10.1016/j.sandf.2017.11.012.

Hirayama, H., 1990. Load-Settlement Analysis for Bored Piles Using Hyperbolic Transfer Functions. Soils Found. 30 (1), 55–64. https://doi.org/10.3208/sandf1972.30.55.

Hsiung, B.-C.-B., Dao, S.-D., 2014. Evaluation of constitutive soil models for predicting movements caused by a deep excavation in sands. Electron. J. Geotech. Eng. 19, 17325–17344.

Huynh, Q.T., Lai, V.Q., Boonyatee, T., Keawsawasvong, S., 2022a. Verification of soil parameters of hardening soil model with small-strain stiffness for deep excavations in medium dense sand in Ho Chi Minh City. Vietnam. Innovative Infrastructure Solutions 7 (1), 15.

Huynh, V.-H., Nguyen, T., Nguyen, D.-P., Nguyen, T.-S., Huynh, T.-M.-D., Nguyen, T.-C., 2022b. A novel direct SPT method to accurately estimate ultimate axial bearing capacity of bored PHC nodular piles with 81 case studies in Vietnam. Soils Found. 62 (4), 101163. https://doi.org/10.1016/j.sandf.2022.101163.

Janbu, N. 1963. Soil compressibility as determined by oedometer and triaxial tests. In: Proceedings of the Proc. European Conf. SMFE, Wiesbaden, 1963. pp. 19-25.

Krasiński, A., Wiszniewski, M., 2017. Static load test on instrumented pile–field data and numerical simulations. Studia Geotechnica et Mechanica 39 (3), 17–25.

Likitlersuang, S., Surarak, C., Wanatowski, D., Oh, E., Balasubramaniam, A., 2013. Finite element analysis of a deep excavation: A case study from the Bangkok MRT. Soils Found. 53 (5), 756–773.

Lim, A., Ou, C.-Y., Hsieh, P.-G., 2010. Evaluation of clay constitutive models for analysis of deep excavation under undrained conditions. J. GeoEng. 5 (1), 9–20.

Liu, J., Xiao, H.B., Tang, J., Li, Q.S., 2004. Analysis of load-transfer of single pile in layered soil. Comput. Geotech. 31 (2), 127–135. https://doi.org/10.1016/j.compgeo.2004.01.001.

Liu, K.-F., Xie, X.-Y., Luo, Z., Hu, Q.-H., Huang, C.-X., 2017. Full-scale field load testing of long drilled shafts with enlarged base constructed in marine sediment. Mar. Georesour. Geotechnol. 35 (3), 346–356. https://doi.org/10.1080/1064119X.2016.1172684.

Meyerhof George, G., 1976. Bearing Capacity and Settlement of Pile Foundations. J. Geotech. Eng. Div. 102 (3), 197–228. https://doi.org/10.1061/AJGEB6.0000243.

Mohurd, G.B. 2011. 50007-2011 - Code for Design of Building Foundation. China Architecture & Building Press.

Nguyen, B.-P., Nguyen Thanh, T., Nguyen Thi Hai, Y., Tran, T.-D., 2022. Performance of composite PVD–SC column foundation under embankment through plane-strain numerical analysis. Int. J. Geomech. 22 (9), 04022155. https://doi.org/10.1061/(ASCE)GM.1943-5622.0002494.

Nguyen, T.T., Le, V.D., Huynh, T.Q., Nguyen, N.H.T., 2024. Influence of settlement on base resistance of long piles in soft soil—field and machine learning assessments. Geotechnics 4 (2), 447–469. https://doi.org/10.3390/geotechnics4020025.

Said, I., De Gennaro, V., Frank, R., 2009. Axisymmetric finite element analysis of pile loading tests. Comput. Geotech. 36 (1), 6–19. https://doi.org/10.1016/j.compgeo.2008.02.011.

Schanz, T., Vermeer, P., and Bonnier, P.G. 2019. The hardening soil model: formulation and verification. In: Beyond 2000 in computational geotechnics. Routledge. Pp. 281–296.

Schmertmann, J.H. 1978. Guidelines for cone penetration test: performance and design. United States. Federal Highway Administration.

Shaolei, H., Yang, C., Guoliang, D., Weiming, G., 2015. Field test research of inclined large-scale steel pipe pile foundation for offshore wind farms. J. Coast. Res. 73 (sp1), 132–138. https://doi.org/10.2112/SI73-024.1.

Sharo, A., Al-Shorman, B., Bani Baker, M., Nusier, O., Alawneh, A., 2022. New approach for predicting the load-displacement curve of axially loaded piles in sand. Case Stud. Constr. Mater. 17, e01674. https://doi.org/10.1016/j.cscm.2022.e01674.

Sidorov, V., and Almakaeva, A. 2020. Soil and structure interaction investigation features. In: Proceedings of the IOP Conference Series: Materials Science and Engineering. IOP Publishing. p. 072013.

Tamboura, H.H., Isobe, K., Ohtsuka, S., 2022. End bearing capacity of a single incompletely end-supported pile based on the rigid plastic finite element method with non-linear strength property against confining stress. Soils Found. 62 (4), 101182. https://doi.org/10.1016/j.sandf.2022.101182.

TCVN 10304. 2014. Pile Foundation- Design Standard. Vietnam National Standard, Ministry of Science and Technology.

Teo, P., Wong, K., 2012. Application of the Hardening Soil model in deep excavation analysis. The IES Journal Part a: Civil & Structural Engineering 5 (3), 152–165.

Ter-Martirosyan, A., Sidorov, V., and Almakaeva, A. 2019. Determining the interfaces parameters for geotechnical modelling. In: Proceedings of the E3S Web of Conferences. EDP Sciences. p. 04042.

Tra, H.T., Huynh, Q.T., Keawsawasvong, S., 2023. Estimating the ultimate load bearing capacity implementing extrapolation method of load-settlement relationship and 3D-finite element analysis. Transp. Infrastruct. Geotechnol. https://doi.org/10.1007/s40515-023-00332-z.

Von Soos, P., 1990. Properties of soil and rock (in German), Grundbau Taschenbuch part 4. Ernst & Sohn, Berlin.